

Resonant Band-Edge Emissive States in Strongly Confined CsPbBr₃ Perovskite Nanoplatelets

Etienne Socie,* Brener R. C. Vale, Aaron T. Terpstra, Marco A. Schiavon, and Jacques-E. Moser*

Cite This: *J. Phys. Chem. C* 2021, 125, 14317–14325

Read Online

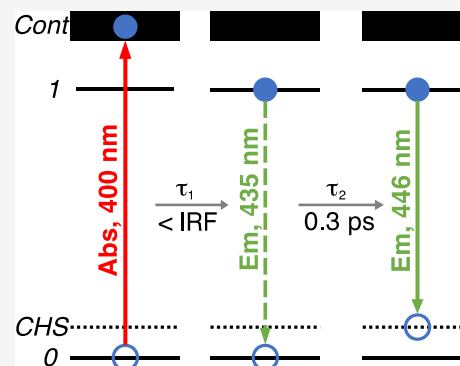
ACCESS |

Metrics & More

Article Recommendations

Supporting Information

ABSTRACT: Strongly confined, fully inorganic cesium lead halide perovskite nanocrystals are of great promise for light-emitting devices in the blue spectral range owing to their high photoluminescence quantum yields. A combination of broadband fluorescence up-conversion and transient absorption spectroscopies was used to study early exciton dynamics in quasi-1D CsPbBr₃ nanoplatelets (3 × 4 × 23 nm³, NPLs). This allowed to reveal emitting band-edge states in the NPLs that form instantaneously upon photoexcitation and then relax within the first picosecond to lower energy confined hole states (CHSs). The influence of the pump excitation intensity on the latter process was further scrutinized. The band-edge population lifetime was found to increase with the rise of the photon fluence due to CHS filling. When the concentration of NPLs in solution becomes very high, nanoparticles overlap, resulting in a decrease in their external absorption cross-section and an increase in the emission Stokes shift due to photon reabsorption.



INTRODUCTION

Hybrid lead halide perovskite nanocrystals (PNCs) have become one of the most attractive materials for optoelectronic applications over the last years. The intrinsic properties of perovskite structures make them promising for light-emitting diodes (LEDs) or lasing.^{1–4} PNCs exhibit a wide band gap tunability (400–700 nm), which is obtained via the halide composition and particle size, narrow photoluminescence (PL) linewidths, and close to unity PL quantum yields.^{5–8} However, due to the instability of chloride compounds, CsPbX₃-based (X = Cl, Br, or I) devices show limited performances in the blue spectral range.^{9–11}

Recently, studies on strongly confined CsPbBr₃ nanocrystals, that is, systems that have at least one dimension smaller than the bulk-exciton Bohr diameter, $a_0 = 7.0$ nm,⁵ such as nanoplatelets (NPLs) or nanowires, exhibited a high-intensity blue emission coming from the recombination of tightly bound excitons (up to few hundreds of meV).^{12–18} The NPL thickness is precisely controlled throughout the synthesis process by adjusting the stoichiometry between the lead and the cesium sources.¹⁹ By decreasing the number of perovskite layers, quantum confinement is increased, which shifts the emission toward the blue region. Although many studies are focusing their efforts on improving the stability and the brightness of perovskite NPLs, there is a lack of understanding about the underlying photophysics.

For example, divergent findings concerning hot-carrier dynamics in PNCs are reported in the literature. Because hot-charge trapping can compete with carrier cooling, it is, therefore, crucial to achieve fast relaxation for LEDs.²⁰ On one hand, slow charge carrier relaxation (up to tens of ps) was

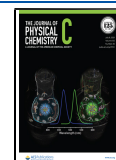
observed at a high photon fluence, mainly for weakly confined systems.^{20–24} Li et al.²¹ suggested that a combination of hot-phonon bottlenecks and Auger-heating effects may be responsible for the lengthening of the cooling dynamics.^{21,25} On the other hand, some studies noted ultrafast cooling for strongly confined NPLs.^{26–29} Hintermayr et al.²⁶ compared hot-carrier dynamics for 3D and 2D methylammonium lead iodide perovskites by using transient absorption spectroscopy (TAS). They reported a fast build-up of the band-edge signal for the 2D system, even when pumping the sample at a high fluence and far above the band edge. The fast dynamics are attributed to the accelerated dissipation of excess energy to phonon emission from the surrounding capping ligands. As the surface-to-volume ratio is higher for strongly confined PNCs, the transfer of phonons into the organic ligands is promoted.

Additionally, some questions need to be answered regarding the origin of the Stokes-shifted emission in strongly confined NPLs. Indeed, to avoid as much as possible photon reabsorption in LEDs, it is essential to have a material with a large intrinsic Stokes shift (ΔE_S). In strongly confined systems, ΔE_S is equal to the difference between the energies of the first excitonic absorption and the static emission peak. Having a Stokes-shifted PL also indicates that different states are

Received: February 13, 2021

Revised: May 11, 2021

Published: June 27, 2021



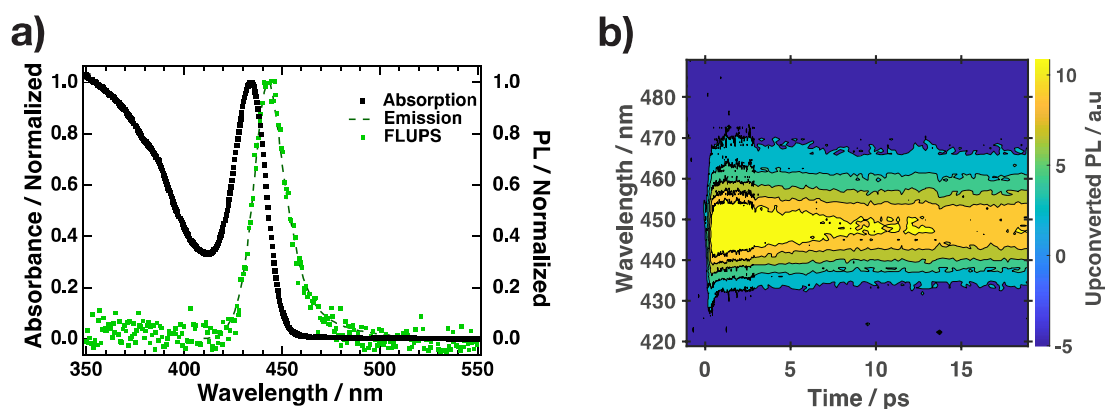


Figure 1. (a) Normalized absorption (black dots), emission (green dashed line) spectra, and the integrated FLUPS signal at the lowest photon fluence (green dots) of CsPbBr₃ NPLs in dodecane. (b) 2D time-resolved emission spectra of CsPbBr₃ acquired by FLUPS ($\lambda_{\text{exc}} = 400$ nm). The low-excitation energy fluence ($38 \mu\text{J cm}^{-2}/\text{pulse}$) corresponded to an average number of photogenerated electron–hole pairs per nanoparticle $\langle N_{\text{ex}} \rangle = 0.1$.

involved during absorption and emission. Theoretical and experimental studies suggest that ΔE_S is due to the existence of a confined hole state (CHS) above the valence band,^{30,31} as already reported in CIS and CdSe quantum dots (QDs).^{32–34} The value of ΔE_S is reported to be increasing with quantum confinement.^{30,31} However, different mechanisms have also been proposed, such as photon reabsorption due to the NPL ensemble size distribution³⁵ or lattice relaxation with the formation of a polaron.³⁶

In this study, we are combining ultrafast transient absorption and broadband fluorescence up-conversion spectroscopies (FLUPS) to investigate the early exciton dynamics in the as-synthesized NPLs. A short-lived emission, overlapped with the first excitonic absorption, is detected by FLUPS, and its decay follows the rise in the main peak. We assign the first emission to the radiative relaxation from the conduction band-edge state to the valence band-edge state, while the main emission corresponds to the relaxation from the conduction band-edge state to CHSs, supporting the conclusions of Brennan et al.^{30,31} Moreover, we study the hole-trapping dynamics of relaxation to CHSs, first by isolating the band-edge emission and second by varying the pump intensity and the sample concentration. We report a slower decay of the band-edge signal at a higher fluence, which can be rationalized by Auger heating, phonon bottleneck, or state filling. Interestingly, the dynamics of the photoinduced absorption (PIA) located on the red side of the TA spectrum, which has previously been attributed to the biexciton-induced Stark effect,^{16,27,28} follows the same dynamics as the band-edge emission observed by FLUPS. Finally, we show that for a highly concentrated solution (with an absorbance $A > 2$ at the band edge), NPLs are overlapping, which decreases the calculated absorption cross-section and leads to photon reabsorption.

METHODS

Synthesis of CsPbBr₃ NNPLs. The synthesis of CsPbBr₃ NPLs has been previously described in full detail.¹⁶ Two precursor solutions were prepared. The lead source was prepared by adding PbBr₂ (0.20 mmol), ZnBr₂ (0.13 mmol), oleic acid (OA, 1 mL), and oleylamine (OAm, 1 mL) together in dodecane (5 mL) in a 50 mL three-necked flask. The solution was dried for 60 min on a Schlenk line and heated under vigorous stirring to 150 °C under an argon atmosphere to solubilize PbBr₂. At the same time, the Cs⁺ cation source

was prepared by mixing Cs₂CO₃ (2.0 mmol), OA (2.5 mL), and octadecene (17.5 mL) in a second 50 mL three-necked flask. The mixture was dried at 120 °C for 60 min and heated to 150 °C under argon for 30 min. Finally, the warm cesium oleate precursor (0.2 mL) was injected into the lead solution at room temperature under stirring. After 20 min, the product was centrifuged at 5000 rpm for 5 min with 5 mL of methyl acetate, and the precipitate was discarded. A second purification step was achieved by adding another 10 mL of methyl acetate to the solution, which was centrifuged for 15 min at 5000 rpm. The purified NPLs were finally dissolved in dodecane (2 mL) and kept at 4 °C.

Optical Measurements. The fresh NPLs were diluted and transferred to a 1 mm-optical pathlength quartz cuvette (Type 61, FireflySci) for static characterization. Ultraviolet–visible absorption spectra were acquired on a PerkinElmer Lambda 950 UV/Vis/NIR spectrometer.

Steady-state PL and time-correlated single photon counting (TCSPC) measurements were carried out on a Horiba Jobin Yvon Fluorolog-3 instrument. The excitation source for TCSPC was a nanoLED N-390 system with a repetition rate of 1 MHz, a pulse duration of 1.3 ns, and an excitation wavelength $\lambda_{\text{exc}} = 390$ nm. The PL detection was performed at 90° relative to the excitation source with a photomultiplier tube.

A broadband fluorescence up-conversion setup (FLUPS, LIOP-TEC) was used for ultrafast time-resolved PL measurements. The pump pulse ($\lambda_{\text{exc}} = 400$ nm) was generated by frequency doubling the output of a chirped pulse-amplified (CPA) Ti:sapphire laser (Libra-HE USP, Coherent) and focused onto a 200 μm spot at the sample position. The gate pulse ($\lambda_G = 1300$ nm) was obtained from a white light-seeded optical parametric amplifier (OPERA-Solo, Coherent). The upconverted fluorescence was generated by type II sum frequency generation in a 100 μm -thick BBO crystal (EKSMa Optics). The signal was dispersed in wavelength using UV grating and sent to a CCD camera (Newton 920, Andor). The time correction for the impulse response function (IRF) was calculated to be 250 fs using the cross-correlation between the pump and the probe. The NPL solutions had an absorbance between 0.3 and 1.6 in a 1 mm cuvette at 400 nm.

For transient absorption, the pump pulse ($\lambda_{\text{exc}} = 389$ nm and 500 Hz repetition rate) was obtained by frequency doubling the output of a CPA Ti:sapphire laser (Clark-MXR, CPA-

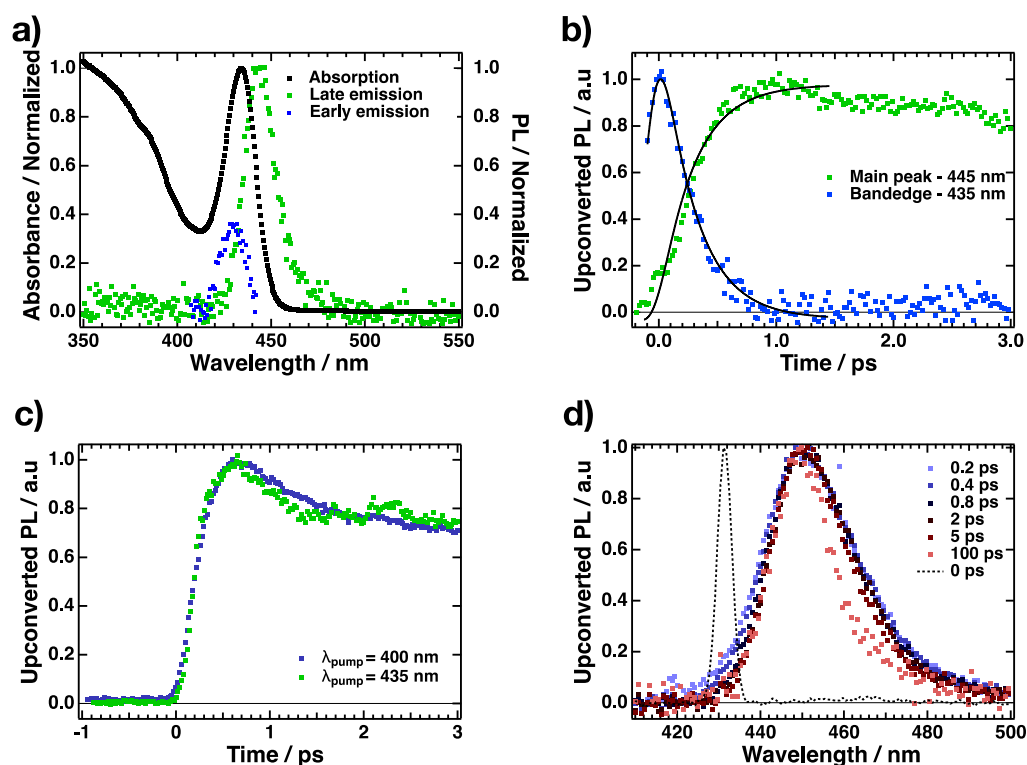


Figure 2. (a) Absorption spectrum (black dots), main emission at 100 ps (green dots), and isolated band-edge emission (blue dots) of CsPbBr₃ NPLs. (b) Main emission dynamics ($\lambda_{\text{probe}} = 445$ nm, green dots) and isolated band-edge emission dynamics ($\lambda_{\text{probe}} = 435$ nm, blue dots) of CsPbBr₃ NPLs in dodecane. (c) Normalized main emission dynamics at 400 nm (blue dots) and 435 nm (green dots) pump wavelengths. (d) Normalized time-resolved emission spectral slices of CsPbBr₃ acquired by FLUPS ($\lambda_{\text{exc}} = 430$ nm) for $\langle N_{\text{ex}} \rangle = 3.3$ and the signal obtained at time zero from the up-conversion of the transmitted pump beam.

2001), and a white-light continuum probe beam ($\lambda_{\text{wl}} = 400$ – 780 nm, 1 kHz repetition rate) was generated by focusing a part of the laser fundamental output at $\lambda = 778$ nm onto a CaF₂ crystal. The white-light probe beam was made smaller and weaker than the pump beam to ensure homogeneity within the probed area. The signal and the reference were sent into a spectrograph (Spectra Pro 2150i, Princeton Instruments) and detected shot-to-shot using a CCD camera (Hamamatsu S07030-0906). The time resolution of the experiment was determined to be 250 fs.

RESULTS & DISCUSSION

The synthesis and standard characterization of strongly confined CsPbBr₃ NPL solutions have been discussed in a previous study.¹⁶ The shape of fresh NPLs is close to that of nanorods ($3 \times 4 \pm 2 \times 26 \pm 6$ nm³) as seen in the TEM images shown in the Supporting Information (Figure S1) and suggests that the quantum confinement of the charges is applied in one to two dimensions. The linear absorption spectrum (Figure 1a) displays a strong and sharp excitonic feature at 435 nm due to quantum confinement. The NPL thickness distribution is homogeneous because the second derivative of the absorption spectrum (Supporting Information, Figure S2) has only one local minimum at 435 nm and is flat from 465 to 600 nm. By fitting the absorption spectrum with a well-known quantum well model (see Supporting Information, Section S1 and Figure S3),^{37,38} we estimate the exciton binding energy to be 318 meV, which is in the range of previous calculations.¹⁶

Figure 1a also shows the NPL static emission spectrum and the integrated FLUPS signal at a low fluence, which are both

centered at 446 nm. The sharp emission (full width at half maximum = 110 meV) is indicative of a weak exciton–phonon coupling, as already reported for strongly confined perovskite NPLs.³⁹ Here, the value of ΔE_{S} , 59 meV (11 nm), is smaller than the theoretical value for QDs with the same radius³⁰ because the synthesized NPLs are not confined equally in each dimension. However, at this point, some questions can be raised: is there only one emitting state? Why is the band-edge emission invisible in the static measurement? Is it possible to track the sub-picosecond dynamics of the photogenerated charge carriers?

Here, we used the fluorescence up-conversion technique to obtain information on early excited-state dynamics. Because the time-resolved photoluminescence (TRPL) signal only depends on the excited-state population, it is, therefore, more straightforward to interpret than TAS spectra. The main advantage of FLUPS over other TRPL techniques is that the time resolution of the setup is only limited by the laser pulse duration. Moreover, the used FLUPS setup was broadband and allowed for scan-free measurements, leading to 2D time-resolved emission spectra, as displayed in Figure 1b. All measurements were carried out at room temperature on fresh colloidal NPL solutions, with the optical pump set at $\lambda_{\text{exc}} = 400$ nm (see the Methods section). Figure 1b shows the obtained TRPL signal when the NPLs were pumped at the lowest fluence, which should produce much less than one exciton per particle. The FLUPS signal has a maximum at 446 nm, and the dynamics of the main peak matches the ones on the red side ($\lambda_{\text{probe}} = 460$ nm) of the PL, as shown in the Supporting Information (Figure S4a). This indicates that the emission

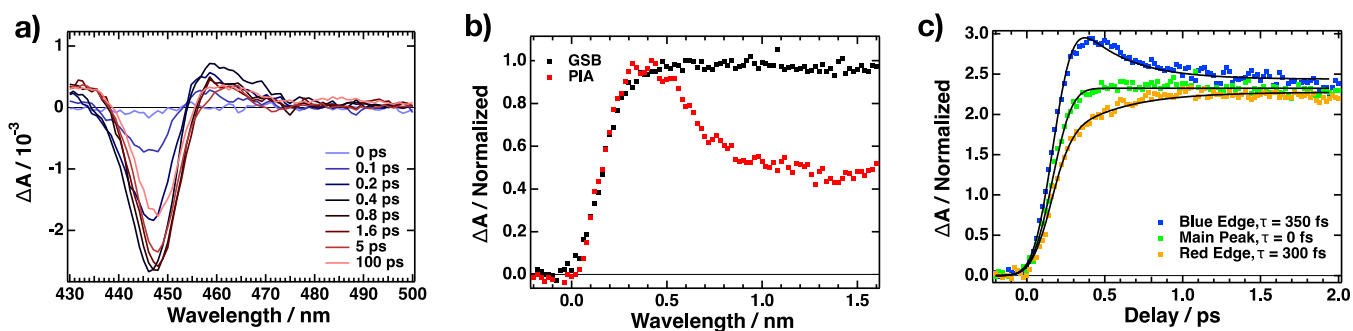


Figure 3. (a) TA spectral slices of CsPbBr₃ NPLs ($\lambda_{\text{exc}} = 390$ nm) for $\langle N_{\text{ex}} \rangle = 0.2$. The extracted GSB dynamics were taken at 2.77 eV and the PIA at 2.84 eV. (b) PIA dynamics (red dots) and GSB dynamics (black dots) obtained from TA experiments at the lowest photon fluence. (c) TA dynamics at three different position around the GSB signal (blue-edge, main peak, and red-edge). These data were normalized at 1880 ps.

does not shift with time and confirms the homogeneous size distribution of the NPLs.^{40,41}

Interestingly, a short-lived feature at approximately 430–435 nm is visible within the first ps of the FLUPS spectrum. To isolate and study the short-lived emission, we subtracted the late-time signal (corresponding to the steady-state emission) from the one at early time (see the detailed procedure in the Supporting Information, Section S2). Figure 2a shows the absorption, the PL at 100 ps, and the isolated short-lived signal (<1 ps). Although the 100 ps emission (referred to as the main emission hereafter) is Stokes-shifted compared to the linear absorption, the short-lived signal overlaps nearly perfectly with the excitonic feature in the absorption spectrum. Therefore, we assign this short-lived signal to the radiative relaxation of the exciton from the conduction band-edge state to the valence band-edge state, which will be called the band-edge emission for the remainder of the text. Figure 2b shows the dynamics of the band edge and the main emission within the first 5 ps. The rise in the band-edge signal is instantaneous, indicating that band-edge excitons are formed faster than the time resolution of the instrumentation. Ultrafast carrier thermalization and cooling have already been reported in such a confined system, suggesting that the signal at 435 nm corresponds to the lowest vibrational state.^{16,26–29} Moreover, the low amount of excess energy (0.25 eV) and the low pump photon fluence ($38 \mu\text{J cm}^{-2}$ /pulse) used for this study favor ultrafast carrier cooling. By fitting the band-edge emission with a mono-exponential decay convoluted with the IRF (see the Supporting Information, Section S3 for the fitting procedure), we obtain a lifetime of $\tau = 0.29$ ps. As shown in the Supporting Information (Figure S5), τ is independent of the probed wavelength, which indicates that a unique population state is involved (homogeneous broadening). Interestingly, the band-edge decay also matches the rise in the main emission at 445 nm (Supporting Information, Table S1), which may unveil the relaxation of band-edge excitons to a lower energy state. The difference between the fitting curve and the main peak signal after 1 ps arises from the fast trapping of excitons into dark states, resulting in a PL decay.^{42–44} To ascertain that the rise in the main PL emission is not linked to the cooling of hot carriers, we also set the pump wavelength to 430 nm, which is close to the lowest excitonic level (Figure 2c). Here, the main peak rise is strictly the same as the one when pumping at higher excitation energy. Moreover, the band-edge emission is still visible around 435 nm at the highest energy fluence (Figure 2d). Because band-edge states are the only states populated upon 430 nm excitation, the short-lived emission

cannot be explained by the recombination of higher excited excitons.

This signal is, however, overlapped with a part of the transmitted pump beam around time zero, which makes the analysis of the dynamics impossible. This state has already been assigned as a CHS and is used to explain the size dependence of ΔE_s in PNCs.^{30,31} Therefore, we suggest that in strongly confined NPLs, hot-carrier cooling to the band edge is ultrafast (faster than the time resolution of the setup) and the hole confinement into CHSs happens subsequently in 290 ± 20 fs at a low fluence. Our TAS measurements reveal ground-state bleaching (GSB) close to the band edge of the linear absorption spectrum, and PIA occurs at a lower energy than GSB, which decays quickly within approximately 270 ± 20 fs (Figure 3a). This PIA peak has been previously assigned to the biexciton-induced Stark effect,^{16,27,28,45} which takes place prior to thermalization and cooling. According to the literature, the cooling in PNCs can be measured by the rise in the GSB extent or the decay of PIA.^{27,28,45} However, in this case, the GSB build-up time is faster than the PIA decay, as displayed in Figure 3b. The GSB rise agrees well with the data obtained by FLUPS, indicating that hot-carrier cooling in CsPbBr₃ NPLs is faster than FLUPS and the TAS time resolution, which our fittings have found to be rise-limited to the IRF, < 200 fs. We also extracted the carrier temperature (T_c) by fitting the high-energy tail of the TA spectrum (see the Supporting Information, eq S5). It is well known that the effective masses of electrons and holes are roughly equal in halide perovskites, which means that the electron temperature (T_e) is considered the same as the hole temperature (T_h). T_c represents an average temperature of electrons and holes. We used an electronic excess energy of 0.35 eV for the TAS experiment after absorbing a photon energy of 3.2 eV (390 nm), which is equally distributed between the electron and hole. The temperature corresponding to the thermal energy $E = 1.5 k_B T = 0.17$ eV is ~ 1300 K.^{27,28,45} The carrier temperature at a low pump fluence ($\langle N_{\text{ex}} \rangle = 0.2$) at 0.2 ps is measured to be $T_c \approx 350$ K, as shown in the Supporting Information (Figure S6). Weakly confined CsPbBr₃ NCs have a T_c of approximately 1000–2000 K with a cooling time of approximately 0.4 ps when they are excited with extra energy, while CsPbBr₃ NPLs show a similar T_c but with a faster decay rate.^{26,46} Note that the CsPbBr₃ NPLs reported here are much more confined than others reported in the literature, which should make cooling even faster. We did not consider the band gap renormalization to be important here because this process is dominated in the presence of free carriers, likely in bulk

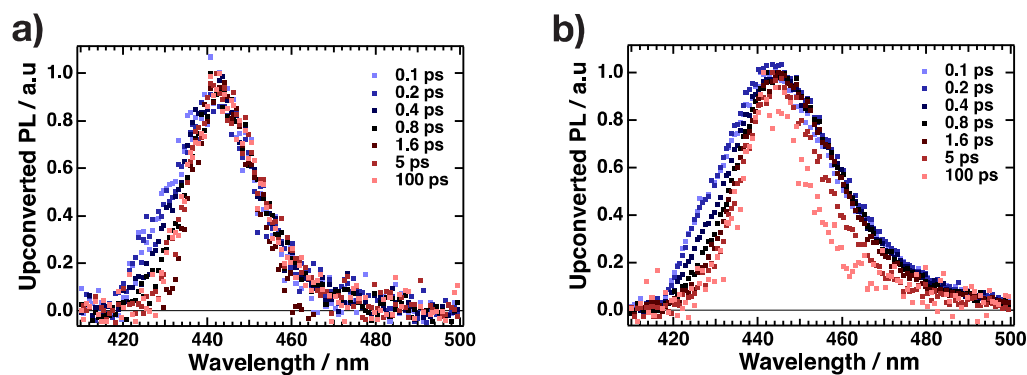


Figure 4. (a) Normalized time-resolved emission spectral slices acquired by FLUPS ($\lambda_{\text{exc}} = 400$ nm) at the lowest ($\langle N_{\text{ex}} \rangle = 0.1$) and (b) the highest photon fluence ($\langle N_{\text{ex}} \rangle = 5.7$).

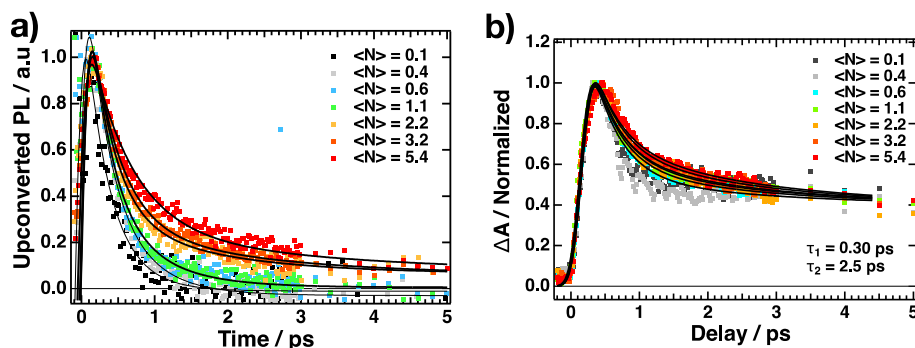


Figure 5. (a) Normalized PL decays of the isolated band-edge emission for $\langle N_{\text{ex}} \rangle = 0.1$ –5.7. (b) PIA dynamics for $\langle N_{\text{ex}} \rangle = 0.2$ –4.

semiconductors, and it occurs faster than the time resolution of our experiment (~ 200 fs).⁴⁷ Nevertheless, the NPLs reported here showed a large exciton binding energy of ~ 350 meV. As it is well known that the exciton transition roughly maintains the absolute energy with increasing photofluence until the binding energy vanishes at the Mott density. Usually, a red or blue shift in the exciton transition is observed with increasing fluence in narrow quantum wells due to the decrease in the band gap energy or decrease in the exciton binding energy, respectively.⁴⁸ However, we did not observe an appreciable shift in the TA spectrum at 0.3 ps with different excitation energy fluences, revealing the exciton stability under these conditions (see the Supporting Information, Figure S7). If the biexciton-induced Stark effect peak decay reflects hot-carrier cooling, we should not observe the PIA peak or it should at least decay faster. Moreover, the PIA decay follows the same dynamics as those of the band-edge emission observed by FLUPS. Our interpretation for the origin of the PIA suggests that this signal has a minor contribution from the exciton–exciton interaction due to the faster cooling and a major contribution from the transition of electrons in the CHS into the conduction band edge, denoted here as CHS–CB. When the hole is trapped into the CHS, the transition CHS–CB is blocked. Therefore, the PIA-decay time constant is due to the hole-trapping rate. According to our proposed mechanism, we should observe a GSB decay with the same lifetime as the one observed for the PIA peak. However, as shown in Figure 3b, the GSB dynamics is flat in this time window. In order to get more information, we probed the dynamics few meV above (blue-edge) and below (red-edge) the GSB minimum (Figure 3c). At short wavelengths, we observe an instantaneous rise and an ultrafast decay of 300 fs, while at longer wavelengths, the rise is

lengthened and has, as well, a 300-fs component. At the minimum of the GSB signal, the rise is instantaneous and no decay is present, which suggests that it displays an average between the two edges. Moreover, we observed in Figure S4 that the three decay curves follow the same trend at longer timescales, indicating that the signal comes from the same set of population. We interpret this result as a contribution of VB–CB and CHS–CB transitions. Because of their large bandwidths, the signals are overlapped. However, as the probed energy moves to the blue edge, we can maximize the VB–CB contribution, while the same happens for the CHS–CB transition when the dynamics are probed at the red edge. Therefore, the fast decay at shorter wavelengths and the rise at longer ones support the hole confinement from band-edge states. The same behavior has been observed in the literature and is ascribed to hole trapping.^{49,50} Here, we can exclude the possibility of charge or energy transfer between different particle sizes because the sample concentration was kept low.⁵¹

Until now, we have discussed the PIA just in terms of time dependence. In addition, the energy dependence agrees well with our interpretation. ΔE_S gives the CHS energy, which is located above the valence band edge, in this case, 58 meV. The biexciton binding energy calculated by FLUPS by following the same subtractive procedure is calculated to be 70 meV. The difference between both quantities, ΔE_S and biexciton binding energy, corresponds to just 2 nm in the region of 445 nm, which is quite reasonable to overlap.

To further study the dynamics of the transfer from the band edge to CHSs, we progressively increased the pump photon fluence from 38 to 955 $\mu\text{J cm}^{-2}$ /pulse in seven steps. The collected spectral slices, at given time delays following excitation at the lowest and the highest fluence, are displayed

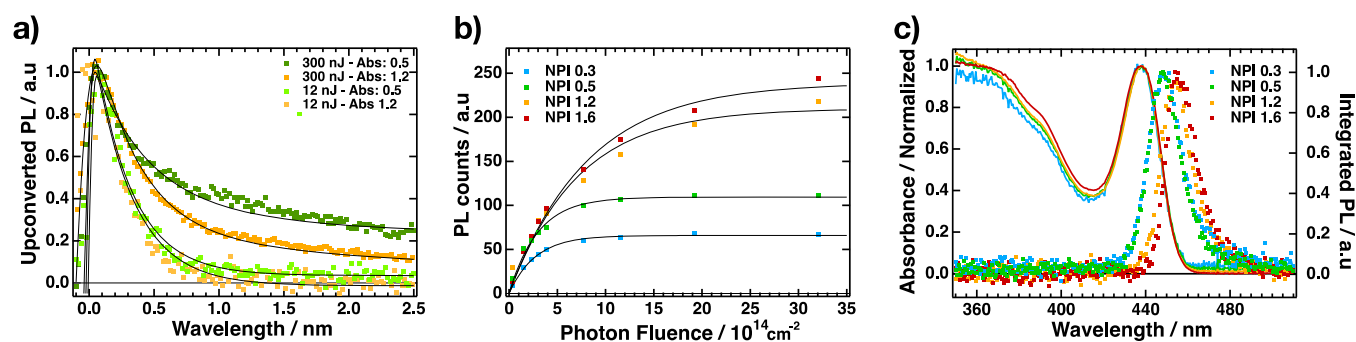


Figure 6. (a) Normalized PL decays of the isolated band-edge emission for different concentrations at $\langle N_{\text{ex}} \rangle = 0.1$ and 5.7. (b) Dependence of the PL intensity on the photon fluence at 100 ps with the fitted Poisson model obtained from eq S7 (Supporting Information) for different concentrations. (c) Absorption (lines) and integrated FLUPS signals (dots) of the CsPbBr₃ NPI solution with absorbances going from 0.3 to 1.6 at $\lambda_{\text{exc}} = 400$ nm.

in Figure 4, while every 2D spectra and spectral slices are shown in the Supporting Information (Figures S8 and S9, respectively). To obtain the average number of excitons per particle generated by the pump pulse, $\langle N_{\text{ex}} \rangle$, we used Poisson statistics (see the procedure in the Supporting Information, Section S4) and found an absorption cross-section $\sigma = 3.4 \times 10^{-15}$ cm² at 400 nm (Supporting Information, Figures S10 and S11a). Consequently, $\langle N_{\text{ex}} \rangle$ varies from 0.1 to 5.7 by increasing the photon fluence. Figure S11b in the Supporting Information shows that the PL intensity is only linear to the average number of excitons per particle when this number is lower than 1. At each fluence value, the band-edge emission is visible within the first ps on the blue edge of the spectrum and is convoluted with the main emission peak, leading to the broadening of the signal. At higher fluences, another feature, with a lifetime of tens of ps, appears on the red side of the spectrum and has already been attributed to biexciton emission.¹⁶ As seen on the spectral slices, the band-edge emission lifetime seems to be enhanced when the fluence is increased.

To highlight the dependence of the band-edge signal dynamics on the photon fluence, we normalized the PL decay of the isolated band-edge emission for $\langle N_{\text{ex}} \rangle = 0.1$ to 5.7 (Figure 5a). Note that the emission appears instantaneously at all fluences, indicating that hot-carrier thermalization and relaxation to the band edge are faster than the time resolution of the setup, even at the highest fluence. We fitted all the isolated emission with a double-exponential decay convoluted with a Gaussian function simulating the IRF (see the procedure in the Supporting Information, Section S6). The best obtained fits are displayed in the Supporting Information (Figure S12), and the extracted parameters are shown in Table S3. At a sufficiently low fluence ($\langle N_{\text{ex}} \rangle \ll 1$), the band-edge decay is fast and mono-exponential with a lifetime $\tau_1 = 330 \pm 30$ fs, as already mentioned in the latter section. However, a second component, $\tau_2 = 1.5$ –2 ps, appears when there is more than one exciton per particle. Its relative amplitude increases with the fluence and reaches 42% at $\langle N_{\text{ex}} \rangle = 5.7$. The same procedure was carried out for the TAS data probed at the PIA peak. All the TA spectral slices are displayed in Figure S13 (Supporting Information). We normalized the TAS decay for $\langle N_{\text{ex}} \rangle = 0.2$ to 4.0 (Figure 5b). We conducted the same fitting procedure with a double-exponential function convoluted with the IRF (Supporting Information, Table S4), and we found a mono-exponential decay behavior for excitation fluences lower than $\langle N_{\text{ex}} \rangle = 1$. At higher fluences, the decay is fitted with a

double-exponential function, and the amplitude related to the second component also increases with the fluence. Many factors might explain the slower relaxation at high fluences: exciton–exciton interactions leading to Auger heating,^{21,52} phonon bottlenecks due to the coupling of the NPIs with organic ligands that can dissipate the excess energy,^{21,26} or solely the state-filling effect, because the density of state (DOS) of CHSs is lower.^{29,30} At this point, theoretical models are missing for evaluating the weight of each part. However, because hot-carrier cooling to the band edge in strongly confined perovskite NCs is independent of the fluence, Auger heating and phonon bottlenecks are less likely to be able to explain the slower relaxation to CHSs. Hence, we expect that state filling may be the critical step. To support this argument, Brennan et al. suggested that the ratio between the DOS in the conduction band edge and CHSs could be as high as 50.³⁰

Finally, we conducted FLUPS measurements on suspensions with different NPI concentrations to be able to rule out photon reabsorption as a cause of the Stokes-shifted emission. Four samples were prepared from the same batch, whose absorption spectra are shown in the Supporting Information, Figure S14. The samples will be named NPI-0.3, NPI-0.5, NPI-1.2, and NPI-1.6 in the following, according to their absorbance measured at $\lambda = 400$ nm. All the absorption spectra overlap, meaning that the optical properties remain unaffected upon dilution. For each sample, the pump energy is set to 12 nJ per laser pulse (fluence = $38 \mu\text{J cm}^{-2}$ /pulse) and 300 nJ/pulse (fluence = $955 \mu\text{J cm}^{-2}$ /pulse). The 2D time-resolved emission spectra and the spectral slices at a given time delay following excitation are shown in the Supporting Information, Figures S15 and S16. As seen in Figure S16, at the lowest pump fluence, the PL peak does not shift with time, ruling out the formation of bigger NPIs through aggregation when the concentration is increased. When the pump fluence is increased to 300 nJ, an additional emission, red shifted compared to the main peak, appears. This has been already attributed to the biexciton signature.¹⁶ Figure 6a displays the normalized PL decay of the isolated band-edge emission for NPI-0.5 and NPI-1.2 at both a low and high fluence. Under a high excitation intensity, the population decay of the band-edge exciton is faster for the concentrated solution than for the dilute solution. Table S5 summarizes the obtained decay lifetimes and their relative weights for the four traces. As reported in the last section, the two decay components, $\tau_1 = 0.32$ ps and $\tau_2 = 2.1$ ps, are independent of the fluence not the concentration. However, under high pump fluence, the relative

amplitude of τ_2 decreases when the NPL concentration is increased.

To explain this observation, we calculated the average interparticle distance $\langle d \rangle$ between two NPLs (see the Supporting Information, Section S7) and found $\langle d \rangle = 37$ nm and 67 nm for the concentrated and the dilute solution, respectively. Consequently, in the former solution, the average distance between two particles is smaller than twice the NPL average length (46 nm), suggesting that we may have an overlap between NPLs. In colloidal solutions, if the NPLs are overlapped, they cast a shadow on each other, breaking the conditions that need to be fulfilled for the Beer–Lambert law to be valid. Therefore, we expect a decrease in the extrinsic absorption cross-section, related to the global absorption of light from the sample, for highly concentrated solutions. The extrinsic absorption cross-section of the NPLs in each solution is obtained by the same procedure as described earlier, in which the emission at 100 ps is recorded at different fluences. The dependence of the PL intensity on the fluence and the fitted Poisson models is shown in Figure 6b. The extrinsic absorption cross-section σ values obtained from the fits are displayed in Table 1. There is a noticeable decrease in σ when

Table 1. Absorbance A at the Pump Wavelength $\lambda = 400$ nm, the Extrinsic Absorption Cross-Section σ at the Same Wavelength, Mean Interparticle Distance $\langle d \rangle$, and the Average Number of Excitons per NPL $\langle N_{\text{ex}} \rangle$ for Different Concentrations of CsPbBr₃ NPL Solutions and Excitation Energies per Pulse

	A_{400}	σ_{400} [cm ²]	$\langle d \rangle$ [nm]	$\langle N_{\text{ex}} \rangle$ 12 nJ/pulse	$\langle N_{\text{ex}} \rangle$ 300 nJ/pulse
NPL-0.3	0.3	3.7×10^{-15}	81	0.3	7.1
NPL-0.5	0.5	3.4×10^{-15}	67	0.3	6.5
NPL-1.2	1.2	1.4×10^{-15}	37	0.1	2.7
NPL-1.6	1.6	1.2×10^{-15}	32	0.1	2.2

the mean inter-distance between NPLs is close to or less than twice the NPL length. Even more, the obtained σ values for NPL-1.2 and NPL-1.6 are overestimated because we do not reach the plateau at the highest fluence. Because σ is smaller for NPL-1.2 and NPL-1.6 than for NPL-0.3 and NPL-0.5, the average number of excitons per particle generated by the same pump fluence will decrease as well (Table 1). From the latter section, we already highlighted the slower decay of the band-edge signal when $\langle N_{\text{ex}} \rangle$ increases. Remarkably, going back to Table S2 and S4 (Supporting Information), one can notice that the weights of A_1 and A_2 reported at the highest fluence for NPL-1.2 are close to the values obtained in Table S2 with $\langle N_{\text{ex}} \rangle = 3.2$. Hence, the faster relaxation of the band-edge population for a highly concentrated NPL solution is explained by the decrease in the average number of excitons per particle upon photoexcitation.

Remarkably, the PL is slightly red shifted for NPL-1.2 and NPL 1.6 (Figure 6c). In addition, we can see that the relative intensity of the band-edge emission decreases for NPL-1.2 and even cancels out for NPL-1.6 (Supporting Information, Figure S16). These observations, combined with the calculation of the mean interparticle distance, might point out photon recycling for highly concentrated solutions. In this case, CsPbBr₃ NPLs are packed together and tend to behave as films.^{52–54} Larger NPLs have a narrower band gap and can reabsorb the emitted photon from the smaller ones, enlarging ΔE_{S} .³⁵ Because the

emission of NPL-1.6 is not shifted with time, the reabsorption should be fast and efficient. Indeed, a photon cascade has already been observed in 2D perovskite films having different numbers of layers, and multiple emission peaks were visible.^{51,55,56} This is supported by the decay associated spectrum (DAS) (Supporting Information, Figure S17) obtained by globally fitting the FLUPS signal, in which all the amplitudes have their maximum at the same wavelength. Because photon recycling is faster than the IRF, it cannot explain the observed short-lived emission ($\tau = 300$ fs) when the NPL concentration is kept low enough. To summarize, photon recycling increases the external Stokes shift when the NPL concentration is high but has only a minor impact in dilute solutions, as already mentioned by Gan et al.³⁵

CONCLUSIONS

By combining FLUPS and TA measurements on the as-synthesized strongly confined perovskite NPLs, we unveiled the presence of a short-lived emission overlapping with the excitonic absorption. This signal has been assigned to the recombination of band-edge excitons, and its decay matches the rise in the main emission, corroborating the suggestion of a CHS, which explains the Stokes-shifted emission in PNCs. Although TA data are often difficult to interpret due to the overlap between multiple contributions, FLUPS is more appropriate to study hole confinement because its signal depends only on the excited population. We also investigated the dependence of the band-edge emission dynamics on the photon fluence and found that at high pump intensities, the band-edge PL lifetime is enhanced, possibly due to the state filling of CHSs. Finally, we showed that for highly concentrated solutions, the NPLs are packed together and start to interact with each other, decreasing the absorption cross-section and photon recycling extent. This study not only unveils for the first time, the band-edge emission from strongly confined NPLs but also shows the utility of combining ultrafast spectroscopic methods to understand the photophysical processes in semiconductor materials.

ASSOCIATED CONTENT

Supporting Information

The Supporting Information is available free of charge at <https://pubs.acs.org/doi/10.1021/acs.jpcc.1c01353>.

TEM images and NPLs dimension histograms, quantum well model, Poisson statistics, band-edge emission isolation, fitting procedure, calculation of the mean interparticle distance, DAS, broadband FLUPS 2D spectra, FLUPS spectral slices, and transient absorption spectral slices (PDF)

AUTHOR INFORMATION

Corresponding Authors

Etienne Socie – Photochemical Dynamics Group, Institute of Chemical Sciences & Engineering, École Polytechnique Fédérale de Lausanne, Lausanne CH-1015, Switzerland; Email: etienne.socie@epfl.ch

Jacques-E. Moser – Photochemical Dynamics Group, Institute of Chemical Sciences & Engineering, École Polytechnique Fédérale de Lausanne, Lausanne CH-1015, Switzerland; orcid.org/0000-0003-0747-4666; Email: je.moser@epfl.ch

Authors

Brener R. C. Vale – Photochemical Dynamics Group, Institute of Chemical Sciences & Engineering, École Polytechnique Fédérale de Lausanne, Lausanne CH-1015, Switzerland; Grupo de Pesquisa Química de Materiais, Departamento de Ciências Naturais, Universidade Federal de São João del-Rei, São João del-Rei 36301-160, Minas Gerais, Brazil

Aaron T. Terpstra – Photochemical Dynamics Group, Institute of Chemical Sciences & Engineering, École Polytechnique Fédérale de Lausanne, Lausanne CH-1015, Switzerland

Marco A. Schiavon – Grupo de Pesquisa Química de Materiais, Departamento de Ciências Naturais, Universidade Federal de São João del-Rei, São João del-Rei 36301-160, Minas Gerais, Brazil; orcid.org/0000-0002-1553-5388

Complete contact information is available at:
<https://pubs.acs.org/10.1021/acs.jpcc.1c01353>

Notes

The authors declare no competing financial interest.

ACKNOWLEDGMENTS

Financial support by the Swiss National Science Foundation (SNF, grant no. 200021_175729) and the National Center of Competence in Research “Molecular Ultrafast Science and Technology” (NCCR-MUST), a research instrument of the SNF, is gratefully acknowledged. B.R.C.V. thanks the Swiss Confederation for a Swiss Government Excellence Scholarship and the Federal University of São João del-Rei for support.

REFERENCES

- (1) Lin, K.; Xing, J.; Quan, L. N.; de Arquer, F. P. G.; Gong, X.; Lu, J.; Xie, L.; Zhao, W.; Zhang, D.; Yan, C.; et al. Perovskite Light-Emitting Diodes with External Quantum Efficiency Exceeding 20 per Cent. *Nature* **2018**, *562*, 245–248.
- (2) Cao, Y.; Wang, N.; Tian, H.; Guo, J.; Wei, Y.; Chen, H.; Miao, Y.; Zou, W.; Pan, K.; He, Y.; et al. Perovskite Light-Emitting Diodes Based on Spontaneously Formed Submicrometre-Scale Structures. *Nature* **2018**, *562*, 249–253.
- (3) Kang, C. H.; Dursun, I.; Liu, G.; Sinatra, L.; Sun, X.; Kong, M.; Pan, J.; Maity, P.; Ooi, E.-N.; Ng, T. K.; et al. High-speed colour-converting photodetector with all-inorganic CsPbBr₃ perovskite nanocrystals for ultraviolet light communication. *Light: Sci. Appl.* **2019**, *8*, 94.
- (4) Gong, M.; Sakidja, R.; Goul, R.; Ewing, D.; Casper, M.; Stramel, A.; Elliot, A.; Wu, J. Z. High-Performance All-Inorganic CsPbCl₃ Perovskite Nanocrystal Photodetectors with Superior Stability. *ACS Nano* **2019**, *13*, 1772–1783.
- (5) Protesescu, L.; Yakunin, S.; Bodnarchuk, M. I.; Krieg, F.; Caputo, R.; Hendon, C. H.; Yang, R. X.; Walsh, A.; Kovalenko, M. V. Nanocrystals of Cesium Lead Halide Perovskites (CsPbX₃, X = Cl, Br, and I): Novel Optoelectronic Materials Showing Bright Emission with Wide Color Gamut. *Nano Lett.* **2015**, *15*, 3692–3696.
- (6) Akkerman, Q. A.; Rainò, G.; Kovalenko, M. V.; Manna, L. Genesis, Challenges and Opportunities for Colloidal Lead Halide Perovskite Nanocrystals. *Nat. Mater.* **2018**, *17*, 394.
- (7) Kovalenko, M. V.; Protesescu, L.; Bodnarchuk, M. I. Properties and Potential Optoelectronic Applications of Lead Halide Perovskite Nanocrystals. *Science* **2017**, *358*, 745–750.
- (8) Shamsi, J.; Urban, A. S.; Imran, M.; De Trizio, L.; Manna, L. Metal Halide Perovskite Nanocrystals: Synthesis, Post-Synthesis Modifications, and Their Optical Properties. *Chem. Rev.* **2019**, *119*, 3296–3348.
- (9) Ravi, V. K.; Swarnkar, A.; Chakraborty, R.; Nag, A. Excellent Green but Less Impressive Blue Luminescence from CsPbBr₃ Perovskite Nanocubes and Nanoplatelets. *Nanotechnology* **2016**, *27*, 325708.
- (10) Congreve, D. N.; Weidman, M. C.; Seitz, M.; Paritmongkol, W.; Dahod, N. S.; Tisdale, W. A. Tunable Light-Emitting Diodes Utilizing Quantum-Confined Layered Perovskite Emitters. *ACS Photonics* **2017**, *4*, 476–481.
- (11) Lignos, I.; Protesescu, L.; Emiroglu, D. B.; Maceiczky, R.; Schneider, S.; Kovalenko, M. V.; deMello, A. J. Unveiling the Shape Evolution and Halide-Ion-Segregation in Blue-Emitting Formamidinium Lead Halide Perovskite Nanocrystals Using an Automated Microfluidic Platform. *Nano Lett.* **2018**, *18*, 1246–1252.
- (12) Akkerman, Q. A.; Motti, S. G.; Srimath Kandada, A. R.; Mosconi, E.; D’Innocenzo, V.; Bertoni, G.; Marras, S.; Kamino, B. A.; Miranda, L.; De Angelis, F.; et al. Solution Synthesis Approach to Colloidal Cesium Lead Halide Perovskite Nanoplatelets with Monolayer-Level Thickness Control. *J. Am. Chem. Soc.* **2016**, *138*, 1010–1016.
- (13) Weidman, M. C.; Seitz, M.; Stranks, S. D.; Tisdale, W. A. Highly Tunable Colloidal Perovskite Nanoplatelets through Variable Cation, Metal, and Halide Composition. *ACS Nano* **2016**, *10*, 7830–7839.
- (14) Shamsi, J.; Dang, Z.; Bianchini, P.; Canale, C.; Di Stasio, F.; Brescia, R.; Prato, M.; Manna, L. Colloidal Synthesis of Quantum Confined Single Crystal CsPbBr₃ Nanosheets with Lateral Size Control up to the Micrometer Range. *J. Am. Chem. Soc.* **2016**, *138*, 7240–7243.
- (15) Weidman, M. C.; Goodman, A. J.; Tisdale, W. A. Colloidal Halide Perovskite Nanoplatelets: An Exciting New Class of Semiconductor Nanomaterials. *Chem. Mater.* **2017**, *29*, 5019–5030.
- (16) Vale, B. R. C.; Socie, E.; Burgos-Caminal, A.; Bettini, J.; Schiavon, M. A.; Moser, J.-E. Exciton, Biexciton, and Hot Exciton Dynamics in CsPbBr₃ Colloidal Nanoplatelets. *J. Phys. Chem. Lett.* **2019**, *11*, 387–394.
- (17) Shamsi, J.; Kubicki, D.; Anaya, M.; Liu, Y.; Ji, K.; Frohna, K.; Grey, C. P.; Friend, R. H.; Stranks, S. D. Stable Hexylphosphonate-Capped Blue-Emitting Quantum-Confined CsPbBr₃ Nanoplatelets. *ACS Energy Lett.* **2020**, *5*, 1900–1907.
- (18) Liu, Y.; Guo, M.; Dong, S.; Jiao, X.; Wang, T.; Chen, D. Room temperature colloidal synthesis of CsPbBr₃ nanowires with tunable length, width and composition. *J. Mater. Chem. C* **2018**, *6*, 7797–7802.
- (19) Bohn, B. J.; Tong, Y.; Gramlich, M.; Lai, M. L.; Döblinger, M.; Wang, K.; Hoye, R. L. Z.; Müller-Buschbaum, P.; Stranks, S. D.; Urban, A. S.; et al. Boosting Tunable Blue Luminescence of Halide Perovskite Nanoplatelets through Postsynthetic Surface Trap Repair. *Nano Lett.* **2018**, *18*, 5231–5238.
- (20) Chung, H.; Jung, S. I.; Kim, H. J.; Cha, W.; Sim, E.; Kim, D.; Koh, W.-K.; Kim, J. Composition-Dependent Hot Carrier Relaxation Dynamics in Cesium Lead Halide (CsPbX₃, X=Br and I) Perovskite Nanocrystals. *Angew. Chem., Int. Ed.* **2017**, *56*, 4160–4164.
- (21) Li, M.; Bhaumik, S.; Goh, T. W.; Kumar, M. S.; Yantara, N.; Grätzel, M.; Mhaisalkar, S.; Mathews, N.; Sum, T. C. Slow Cooling and Highly Efficient Extraction of Hot Carriers in Colloidal Perovskite Nanocrystals. *Nat. Commun.* **2017**, *8*, 14350.
- (22) Papagiorgis, P.; Protesescu, L.; Kovalenko, M. V.; Othonos, A.; Itskos, G. Long-Lived Hot Carriers in Formamidinium Lead Iodide Nanocrystals. *J. Phys. Chem. C* **2017**, *121*, 12434–12440.
- (23) Mondal, N.; De, A.; Das, S.; Paul, S.; Samanta, A. Ultrafast Carrier Dynamics of Metal Halide Perovskite Nanocrystals and Perovskite-Composites. *Nanoscale* **2019**, *11*, 9796–9818.
- (24) Boehme, S. C.; Brinck, S. t.; Maes, J.; Yazdani, N.; Zapata, F.; Chen, K.; Wood, V.; Hodgkiss, J. M.; Hens, Z.; Geiregat, P.; et al. Phonon-Mediated and Weakly Size-Dependent Electron and Hole Cooling in CsPbBr₃ Nanocrystals Revealed by Atomistic Simulations and Ultrafast Spectroscopy. *Nano Lett.* **2020**, *20*, 1819–1829.
- (25) Butkus, J.; Vashishtha, P.; Chen, K.; Gallaher, J. K.; Prasad, S. K. K.; Metin, D. Z.; Laufersky, G.; Gaston, N.; Halpert, J. E.; Hodgkiss, J. M. The Evolution of Quantum Confinement in CsPbBr₃ Perovskite Nanocrystals. *Chem. Mater.* **2017**, *29*, 3644–3652.

- (26) Hintermayr, V. A.; Polavarapu, L.; Urban, A. S.; Feldmann, J. Accelerated Carrier Relaxation through Reduced Coulomb Screening in Two-Dimensional Halide Perovskite Nanoplatelets. *ACS Nano* **2018**, *12*, 10151–10158.
- (27) Li, Y.; Lai, R.; Luo, X.; Liu, X.; Ding, T.; Lu, X.; Wu, K. On the Absence of a Phonon Bottleneck in Strongly Confined CsPbBr₃ Perovskite Nanocrystals. *Chem. Sci.* **2019**, *10*, 5983–5989.
- (28) Cong, M.; Yang, B.; Chen, J.; Hong, F.; Yang, S.; Deng, W.; Han, K. Carrier Multiplication and Hot-Carrier Cooling Dynamics in Quantum-Confined CsPbI₃ Perovskite Nanocrystals. *J. Phys. Chem. Lett.* **2020**, *11*, 1921–1926.
- (29) Gramlich, M.; Bohn, B. J.; Tong, Y.; Polavarapu, L.; Feldmann, J.; Urban, A. S. Thickness-Dependence of Exciton-Exciton Annihilation in Halide Perovskite Nanoplatelets. *J. Phys. Chem. Lett.* **2020**, *11*, 5361–5366.
- (30) Brennan, M. C.; Herr, J. E.; Nguyen-Beck, T. S.; Zinna, J.; Draguta, S.; Rouvimov, S.; Parkhill, J.; Kuno, M. Origin of the Size-Dependent Stokes Shift in CsPbBr₃ Perovskite Nanocrystals. *J. Am. Chem. Soc.* **2017**, *139*, 12201–12208.
- (31) Brennan, M. C.; Forde, A.; Zhukovskiy, M.; Baublis, A. J.; Morozov, Y. V.; Zhang, S.; Zhang, Z.; Kilin, D. S.; Kuno, M. Universal Size-Dependent Stokes Shifts in Lead Halide Perovskite Nanocrystals. *J. Phys. Chem. Lett.* **2020**, *11*, 4937–4944.
- (32) Knowles, K. E.; Nelson, H. D.; Kilburn, T. B.; Gamelin, D. R. Singlet–Triplet Splittings in the Luminescent Excited States of Colloidal Cu⁺:CdSe, Cu⁺:InP, and CuInS₂ Nanocrystals: Charge-Transfer Configurations and Self-Trapped Excitons. *J. Am. Chem. Soc.* **2015**, *137*, 13138–13147.
- (33) Berends, A. C.; Rabouw, F. T.; Spoor, F. C. M.; Bladt, E.; Grozema, F. C.; Houtepen, A. J.; Siebbeles, L. D. A.; de Mello Donegá, C. Radiative and Nonradiative Recombination in CuInS₂ Nanocrystals and CuInS₂-Based Core/Shell Nanocrystals. *J. Phys. Chem. Lett.* **2016**, *7*, 3503–3509.
- (34) Hughes, K. E.; Hartstein, K. H.; Gamelin, D. R. Photodoping and Transient Spectroscopies of Copper-Doped CdSe/CdS Nanocrystals. *ACS Nano* **2018**, *12*, 718–728.
- (35) Gan, Z.; Chen, W.; Yuan, L.; Cao, G.; Zhou, C.; Huang, S.; Wen, X.; Jia, B. External Stokes Shift of Perovskite Nanocrystals Enlarged by Photon Recycling. *Appl. Phys. Lett.* **2019**, *114*, 011906.
- (36) Guo, Y.; Yaffe, O.; Hull, T. D.; Owen, J. S.; Reichman, D. R.; Brus, L. E. Dynamic Emission Stokes Shift and Liquid-like Dielectric Solvation of Band Edge Carriers in Lead-Halide Perovskites. *Nat. Commun.* **2019**, *10*, 1175.
- (37) Schnabel, R. F.; Zimmermann, R.; Bimberg, D.; Nickel, H.; Lösch, R.; Schlapp, W. Influence of Exciton Localization on Recombination Line Shapes: In_xGa_{1-x}As/GaAs Quantum Wells as a Model. *Phys. Rev. B* **1992**, *46*, 9873–9876.
- (38) Leosson, K.; Jensen, J. R.; Langbein, W.; Hvam, J. M. Exciton Localization and Interface Roughness in Growth-Interrupted GaAs/AlAs Quantum Wells. *Phys. Rev. B* **2000**, *61*, 10322–10329.
- (39) Liu, A.; Bonato, L. G.; Sessa, F.; Almeida, D. B.; Isele, E.; Nagamine, G.; Zagonel, L. F.; Nogueira, A. F.; Padilha, L. A.; Cundiff, S. T. Effect of Dimensionality on the Optical Absorption Properties of CsPbI₃ Perovskite Nanocrystals. *J. Chem. Phys.* **2019**, *151*, 191103.
- (40) De Weerd, C.; Gomez, L.; Zhang, H.; Buma, W. J.; Nedelcu, G.; Kovalenko, M. V.; Gregorkiewicz, T. Energy Transfer between Inorganic Perovskite Nanocrystals. *J. Phys. Chem. C* **2016**, *120*, 13310–13315.
- (41) Singldinger, A.; Gramlich, M.; Gruber, C.; Lampe, C.; Urban, A. S. Nonradiative Energy Transfer between Thickness-Controlled Halide Perovskite Nanoplatelets. *ACS Energy Lett.* **2020**, *5*, 1380–1385.
- (42) Rossi, D.; Qiao, T.; Liu, X.; Khurana, M.; Akimov, A. V.; Cheon, J.; Son, D. H. Size-Dependent Dark Exciton Properties in Cesium Lead Halide Perovskite Quantum Dots. *J. Chem. Phys.* **2020**, *153*, 184703.
- (43) Becker, M. A.; Bernasconi, C.; Bodnarchuk, M. I.; Rainò, G.; Kovalenko, M. V.; Norris, D. J.; Mahrt, R. F.; Stöferle, T. Unraveling the Origin of the Long Fluorescence Decay Component of Cesium Lead Halide Perovskite Nanocrystals. *ACS Nano* **2020**, *14*, 14939–14946.
- (44) Socie, E.; Vale, B. R. C.; Burgos-Caminal, A.; Moser, J. E. Direct Observation of Shallow Trap States in Thermal Equilibrium with Band-Edge Excitons in Strongly Confined CsPbBr₃ Perovskite Nanoplatelets. *Adv. Opt. Mater.* **2021**, *9*, 2001308.
- (45) Mondal, A.; Aneesh, J.; Kumar Ravi, V.; Sharma, R.; Mir, W. J.; Beard, M. C.; Nag, A.; Adarsh, K. V. Ultrafast Exciton Many-Body Interactions and Hot-Phonon Bottleneck in Colloidal Cesium Lead Halide Perovskite Nanocrystals. *Phys. Rev. B* **2018**, *98*, 115418.
- (46) Shukla, A.; Kaur, G.; Babu, K. J.; Ghorai, N.; Goswami, T.; Kaur, A.; Ghosh, H. N. Effect of Confinement on the Exciton and Biexciton Dynamics in Perovskite 2D-Nanosheets and 3D-Nanocrystals. *J. Phys. Chem. Lett.* **2020**, *11*, 6344–6352.
- (47) Price, M. B.; Butkus, J.; Jellicoe, T. C.; Sadhanala, A.; Briane, A.; Halpert, J. E.; Broch, K.; Hodgkiss, J. M.; Friend, R. H.; Deschler, F. Hot-carrier cooling and photoinduced refractive index changes in organic-inorganic lead halide perovskites. *Nat. Commun.* **2015**, *6*, 8420.
- (48) Klingshirn, C. F. *Semiconductor Optics*; Springer-Verlag: Berlin, Heidelberg, 2005.
- (49) Logunov, S.; Green, T.; Marguet, S.; El-Sayed, M. A. Interfacial Carriers Dynamics of CdS Nanoparticles. *J. Phys. Chem. A* **1998**, *102*, 5652–5658.
- (50) Vale, B. R. C.; Socie, E.; Cunha, L. R. C.; Fonseca, A. F. V.; Vaz, R.; Bettini, J.; Moser, J.-E.; Schiavon, M. A. Revealing Exciton and Metal-Ligand Conduction Band Charge Transfer Absorption Spectra in Cu-Zn-In-S Nanocrystals. *J. Phys. Chem. C* **2020**, *124*, 27858–27866.
- (51) Bouduban, M. E. F.; Burgos-Caminal, A.; Ossola, R.; Teuscher, J.; Moser, J.-E. Energy and Charge Transfer Cascade in Methylammonium Lead Bromide Perovskite Nanoparticle Aggregates. *Chem. Sci.* **2017**, *8*, 4371–4380.
- (52) Davis, N. J. L. K.; de la Peña, F. J.; Tabachnyk, M.; Richter, J. M.; Lamboll, R. D.; Booker, E. P.; Wisnivesky Rocca Rivarola, F.; Griffiths, J. T.; Ducati, C.; Menke, S. M.; Deschler, F.; Greenham, N. C. Photon Reabsorption in Mixed CsPbCl₃:CsPbI₃ Perovskite Nanocrystal Films for Light-Emitting Diodes. *J. Phys. Chem. C* **2017**, *121*, 3790–3796.
- (53) Navarro-Arenas, J.; Suárez, I.; Chirvony, V. S.; Gualdrón-Reyes, A. F.; Mora-Seró, I.; Martínez-Pastor, J. Single-Exciton Amplified Spontaneous Emission in Thin Films of CsPbX₃ (X = Br, I) Perovskite Nanocrystals. *J. Phys. Chem. Lett.* **2019**, *10*, 6389–6398.
- (54) Chirvony, V. S.; Sekerbayev, K. S.; Pashaei Adl, H.; Suárez, I.; Taurbayev, Y. T.; Gualdrón-Reyes, A. F.; Mora-Seró, I.; Martínez-Pastor, J. P. Interpretation of the Photoluminescence Decay Kinetics in Metal Halide Perovskite Nanocrystals and Thin Polycrystalline Films. *J. Lumin.* **2020**, *221*, 117092.
- (55) Yuan, M.; Quan, L. N.; Comin, R.; Walters, G.; Sabatini, R.; Voznyy, O.; Hoogland, S.; Zhao, Y.; Beauregard, E. M.; Kanjanaboos, P.; Lu, Z.; Kim, D. H.; Sargent, E. H. Perovskite Energy Funnels for Efficient Light-Emitting Diodes. *Nat. Nanotechnol.* **2016**, *11*, 872–877.
- (56) Williams, O. F.; Guo, Z.; Hu, J.; Yan, L.; You, W.; Moran, A. M. Energy Transfer Mechanisms in Layered 2D Perovskites. *J. Chem. Phys.* **2018**, *148*, 134706.

Supporting Information

Resonant Band Edge Emissive States in Strongly Confined CsPbBr₃ Perovskite Nanoplatelets

Etienne Socie,^{§*} Brener R. C. Vale,^{§°} Aaron T. Terpstra,[§] Marco A. Schiavon,[°] and Jacques-E. Moser^{§*}

[§] Photochemical Dynamics Group, Institute of Chemical Sciences & Engineering, École Polytechnique Fédérale de Lausanne, CH-1015 Lausanne, Switzerland

[°] Grupo de Pesquisa Química de Materiais, Departamento de Ciências Naturais, Universidade Federal de São João Del-Rei, Campus Dom Bosco, 36301-160 São João Del-Rei, Minas Gerais, Brazil

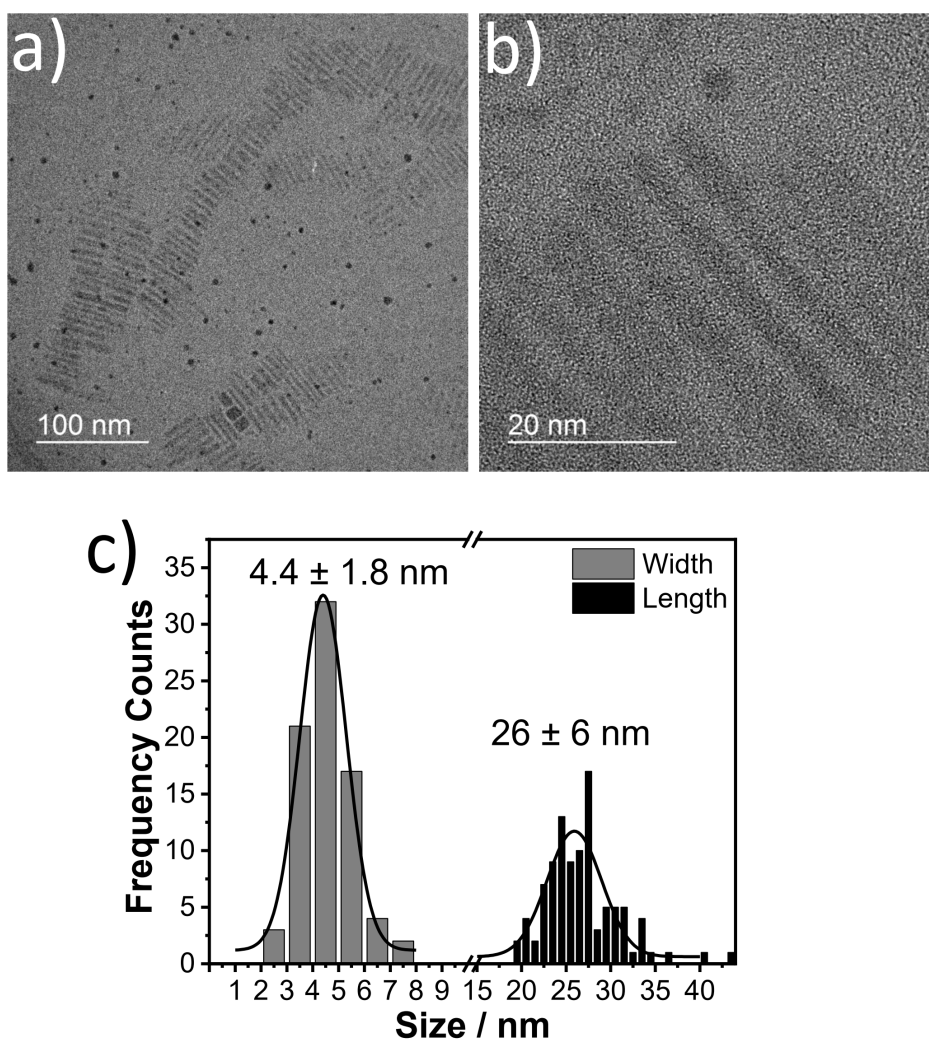


Figure S1. a, b) Transmission electronic microscopy images for two different magnifications. c) Histogram for the width and length of CsPbBr₃ NPLs.

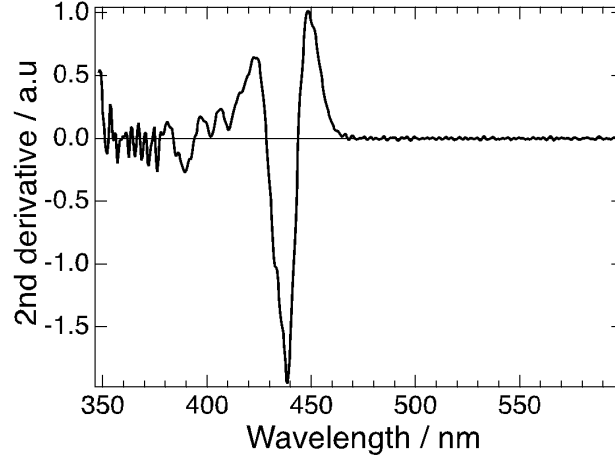


Figure S2. Second derivative of the absorption spectrum of as-synthesized CsPbBr₃ nanoplatelets (NPLs).

S1. Quantum Well Model

The quantum well model (Equation S1) was used to fit the absorption spectrum of CsPbBr₃ NPLs.^{2,3} This model has already been used for CdSe colloidal quantum wells and perovskite NPLs.^{1,4-5}

$$Abs(E) = c\alpha(E) \quad (S1)$$

where $Abs(E)$ is the absorbance from the sample as a function of the energy, $\alpha(E)$ the absorption strength of band edge transitions and c its weight. $\alpha(E)$ is composed of the exciton absorption, $X(E)$ and the continuous band absorption, $Cont(E)$ (Equation S2).

$$\alpha(E) = X(E) + Cont(E) \quad (S2)$$

The two last terms are expressed by Equation S3 and S4.

$$X(E) = \frac{1}{2\eta} \left[ERF \left(\frac{E-E_X}{W_X} - \frac{W_X}{2\eta} \right) + 1 \right] \exp \exp \left(\frac{W_X^2}{4\eta^2} - \frac{E-E_X}{\eta} \right) \quad (S3)$$

$$Cont(E) = \frac{H}{2} \left[ERF \left(\frac{E-E_X-E_b}{W_c} - \frac{W_X}{2\eta} \right) + 1 \right] \quad (S4)$$

where E_x , E_b , W_x , W_c , H and η are the exciton transition energy, exciton binding energy, exciton peak width, continuum edge width, continuum step height and asymmetric broadening respectively.

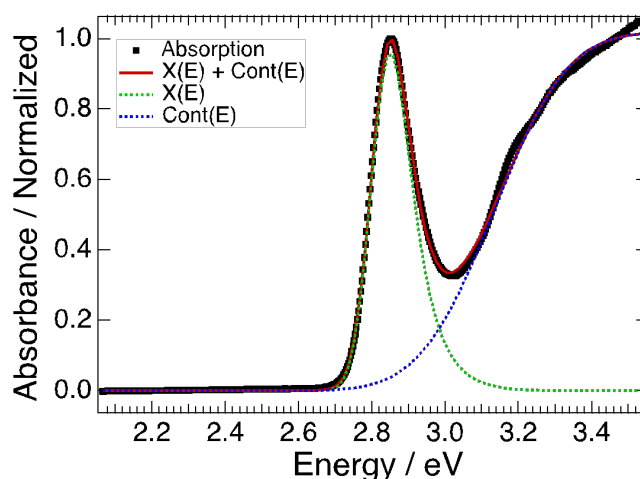


Figure S3. Absorption spectrum of as-synthesized CsPbBr₃ NPIs (black dots), with the best-fitted model used to extract the exciton binding energy (Equation S1, red line), the exciton (Equation S3, green dots) and continuum contributions (Equation S4, blue dots).

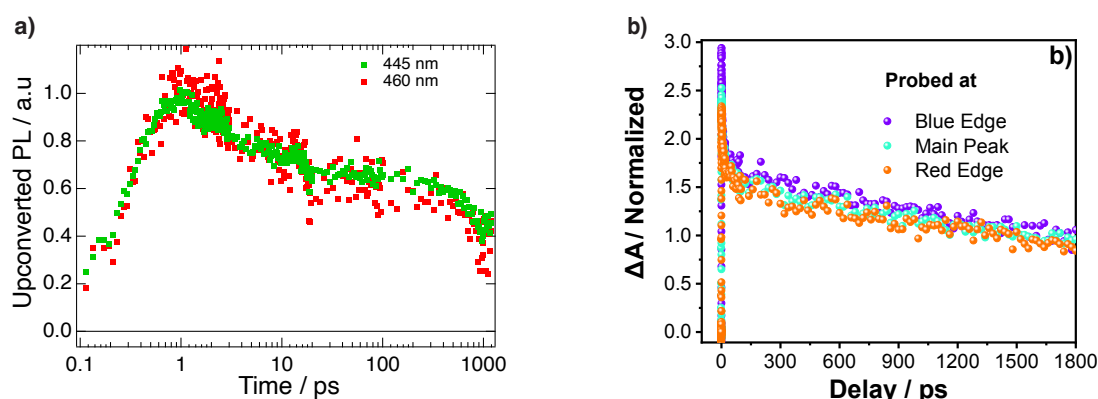


Figure S4. a) Normalized dynamics at the peak position (green dots) and on the red side of the emission (red dots); b) long-timescale of TA dynamics at three different position around the GSB signal (blue-edge, main peak, red-edge). These data were normalized at 1880 ps.

S2. Band Edge Emission Isolation

A homemade MATLAB procedure has been written to isolate and fit the blue-shifted short-lived emission ascribed to recombination from exciton at the band edge (see main text). Firstly, the signal was normalized at the maximum emission for each time delay. Then, we subtracted the normalized signal at early times (0-20 ps) from the normalized signal at the same fluence at 100 ps. An average of 5 spectral slices around 100 ps was used for the subtraction to increase the signal over noise ratio,

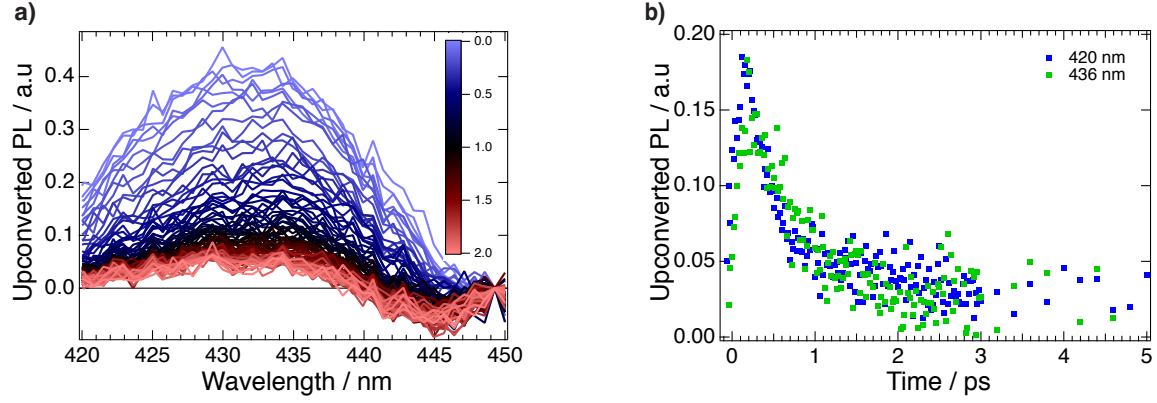


Figure S5. a) Isolated band edge emission spectral slices for CsPbBr₃ pumped at the highest fluence ($\langle N_{ex} \rangle = 5.7$). b) Isolated band edge emission dynamic slices for CsPbBr₃ pumped at the highest fluence ($\langle N_{ex} \rangle = 5.7$).

The procedure for fitting early time signals was carried out by convoluting a Gaussian and exponential function. For decay signals such as PIA and band-edge emission, we have used the equation d, while growth signals such as GSB and main emission peak, we used the equation r.

$$\begin{aligned} \text{Exponential decay:} \quad & d = A_1 \cdot \exp(-t / \tau_1) + A_0 \\ \text{Exponential rise:} \quad & r = A_1 (1 - \exp(-t / \tau_1)) + A_0 \\ \text{Gaussian function:} \quad & g = \left(\frac{B}{((w \cdot \text{sqrt}[\frac{\pi}{2}]))} \right) * \exp[-2 * (\frac{(t-y)}{w})^2] \end{aligned}$$

Table S1. Extracted parameters from the fitted equations displayed in Figure 2b.

Parameters	Band edge	Main peak
A ₁	1.82 ± 0.04	1.33 ± 0.03
w	0.2 ± 0 ps	0.2 ± 0 ps
τ ₁	0.29 ± 0.02 ps	0.29 ± 0.02 ps
t ₀	-0.104 ± 0.006 ps	-0.104 ± 0.006 ps
A ₀	-0.02 ± 0.01	-0.35 ± 0.03
B	1 ± 0	1 ± 0

Table S2. Extracted parameters from the fit equation display in Figure 2c for TA dynamics

Parameters	GSB peak	PIA Peak
A_1	0.955 ± 0.008	1.23 ± 0.05
w	0.25 ± 0 ps	0.25 ± 0 ps
τ_1	0.0036 ± 0.007 ps	0.27 ± 0.02 ps
t_0	0.018 ± 0.009 ps	0.052 ± 0.004 ps
A_0	0 ± 0	0.450 ± 0.009
B	1 ± 0	1 ± 0

S3. Carrier Temperature

For the hot carriers with energies higher than the Fermi Energy Level, the Fermi-Dirac distribution function can be approximated to a Maxwell-Boltzmann distribution, which can be used to extract the carrier temperature by fitting the high-energy tail of TA spectrum.⁶ In this case, we have used the Equation S10.

$$\Delta A = A_1 \exp\left(-\frac{E}{T_c k_B}\right) \quad (\text{S5})$$

Where k_B , E , and T_c are the Boltzmann constant, energy, and carrier temperature, respectively. We selected the energies from 2.85 to 2.95 eV from the TA spectrum at 0.2 ps and at $\langle N_{ex} \rangle = 0.2$. We found a carrier temperature of 350 K.

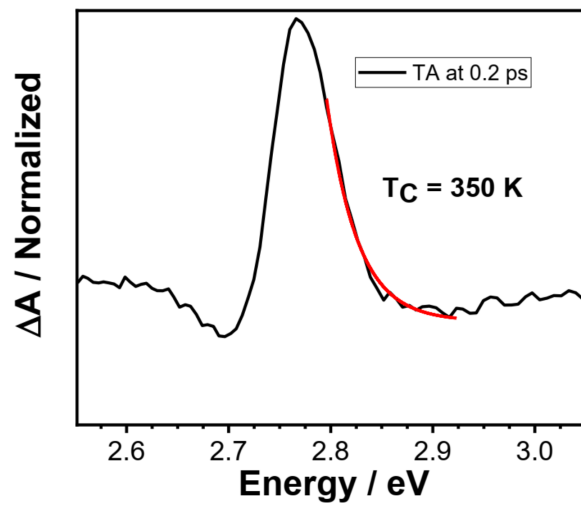


Figure S6. Carrier temperature extracted from the TAS data at 0.2 ps.

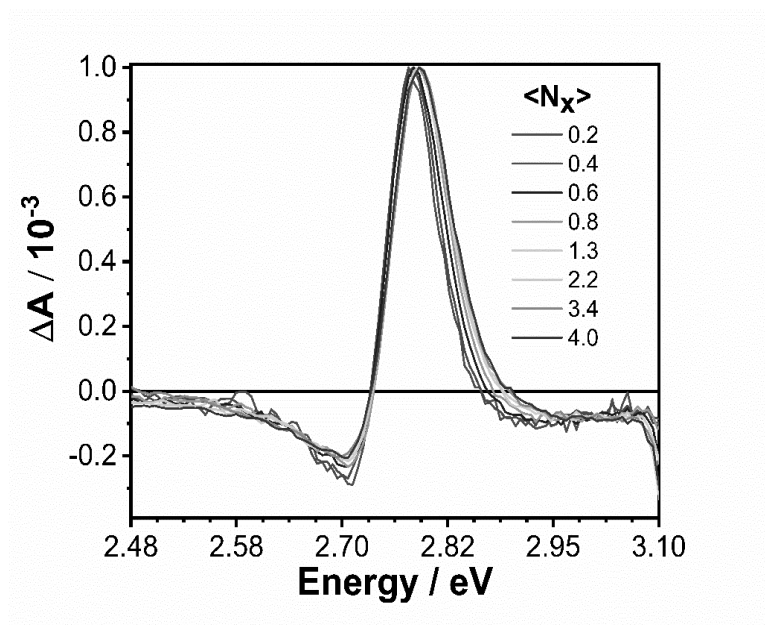


Figure S7. TA spectra recorded at 0.3 ps time delay upon excitation at 390 nm (3.1 eV) with different excitation energy fluences. $\langle N_x \rangle$ is the average number of excitons generated per nanoplatelet.

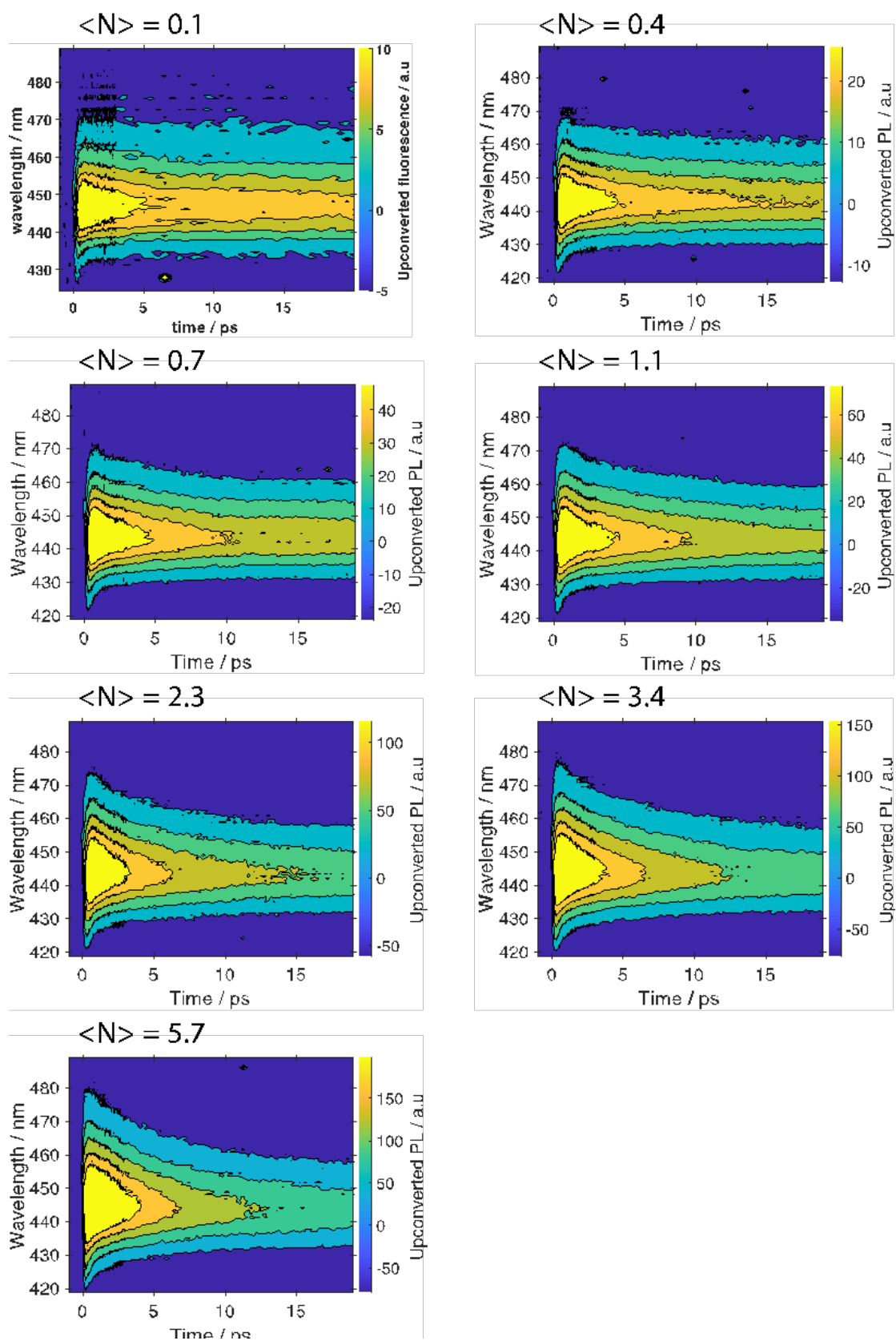


Figure S8. 2D time-resolved emission spectra of CsPbBr₃ acquired by FLUPS ($\lambda_{exc} = 400$ nm) for average numbers of excitons generated by nanoplatelet ranging from $\langle N_{ex} \rangle = 0.1$ to 5.7.

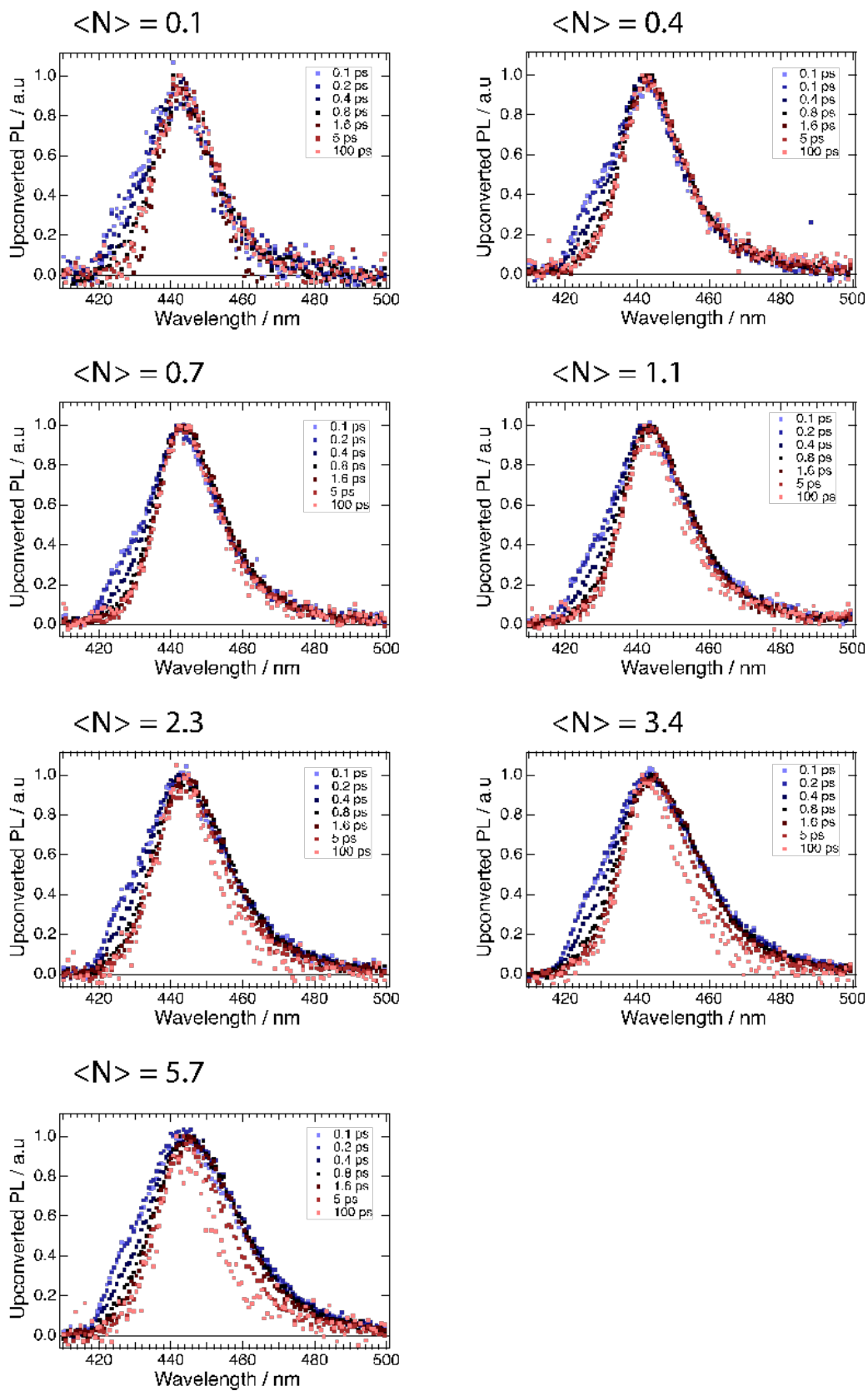


Figure S9. Normalized time-resolved emission spectral slices of CsPbBr₃ acquired by FLUPS ($\lambda_{exc} = 400$ nm) for $\langle N_{ex} \rangle = 0.1 - 5.7$.

S4. Poisson Distribution

The average number of excitons per NPI, $\langle N_{ex} \rangle$, is proportional to both the photon fluence, j , and the absorption cross-section, σ , at a specific wavelength (Equation S6).

$$\langle N_{ex} \rangle = \sigma_{400.nm} \cdot j \quad (S6)$$

To find the value of the absorption cross-section, we used a procedure based on Poisson statistics which has been described elsewhere.^{1,7} The probability of a nanoparticle to contain n excitons is given by Equation S7.

$$P(n) = \frac{\langle N_{ex} \rangle^n \cdot e^{-\langle N_{ex} \rangle}}{n!} \quad (S7)$$

After a long time, all the multi-excitonic events have occurred, and only one exciton can be found per NPI at maximum. Since the PL signal is linear to the number of NPLs containing an exciton, we can plot the intensity emission as a function of the photon fluence of the pump pulse (Equation S8).

$$I(PL, t = 100 \text{ ps}) = A \cdot P(1) = A[1 - P(0)] = A[1 - e^{-\sigma_{400.nm} \cdot j}] \quad (S8)$$

Since the biexciton lifetime as been previously estimated to 10 ps in a similar system,⁵ we fitted for each fluence the spectral slices at 100 ps with a Gaussian function and we displayed the fluence dependence of the amplitude of the Gaussian (Figure S10).

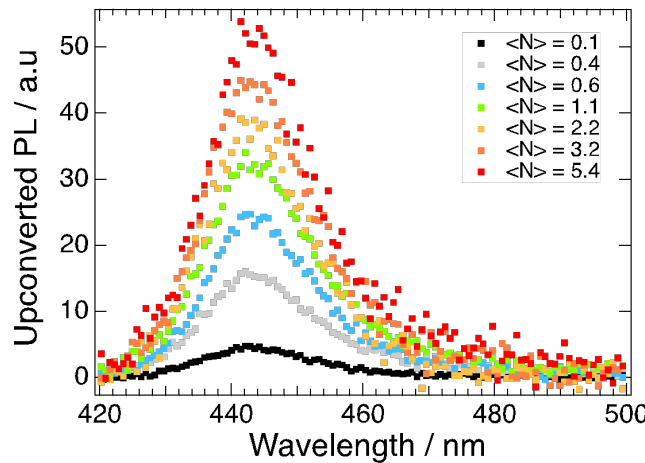


Figure S10. CsPbBr₃ PL spectral slices at 100 ps for $\langle N_{ex} \rangle = 0.1 - 5.4$.

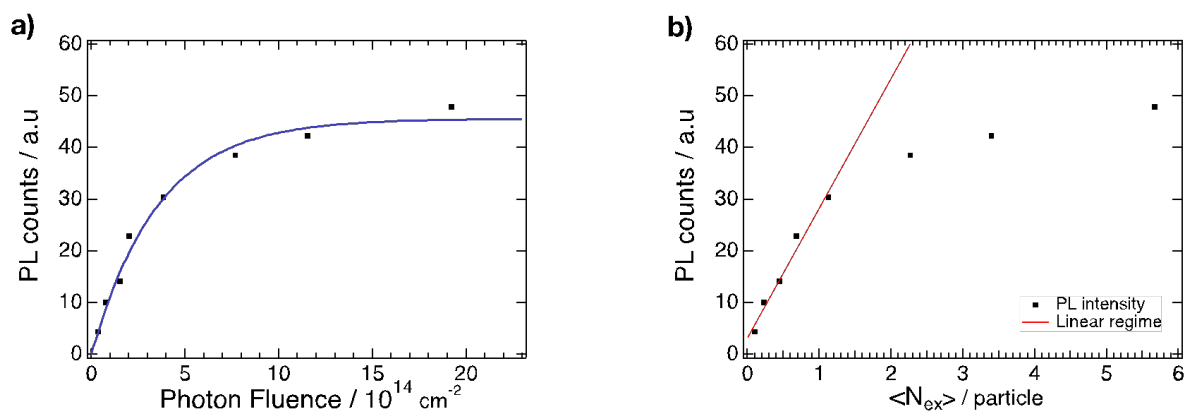


Figure S11. a) Dependence of the PL intensity on the photon fluence at 100 ps (black dots) with the best-fitted Poisson model obtained from Equation S7 (blue line). b) Dependence of the PL intensity on the average number of excitons per particle ($\langle N_{ex} \rangle$) (black dots) with a line illustrating the linear regime when $\langle N_{ex} \rangle$ is lower than 1.

S5. Fitting of the Band Edge Dynamics

Since the dynamics of the band edge emission were similar for each wavelength (Figure S5), an average of 5 dynamic slices was calculated before fitting. Finally, we fitted the PL decays of the isolated band edge emission at each fluence with a mono-exponential (for the lowest photon fluence) or a double exponential function (for the other photon fluences) convoluted with a Gaussian function. The amplitudes and lifetimes were left free, while the Gaussian width and time-zero were fixed. Those values have been extracted from a 2D Gaussian fit using the cross-correlation between the pump and the gate at 400 nm.

Table S3. Extracted amplitude and lifetimes from the fitting procedure described here above.

$\langle N_{ex} \rangle$	0.1	0.4	0.6	1.1	2.2	3.2	5.4
%A ₁	100	97	96	92	81	77	58
%A ₂	-	3	4	8	19	23	42
τ_1 / ps	0.35 ± 0.05	0.36 ± 0.06	0.33 ± 0.03	0.35 ± 0.04	0.32 ± 0.04	0.32 ± 0.03	0.32 ± 0.03
τ_2 / ps	-	1.5 ± 2.71	3.06 ± 2.53	1.47 ± 0.70	1.43 ± 0.35	1.5 ± 0.25	1.99 ± 0.17

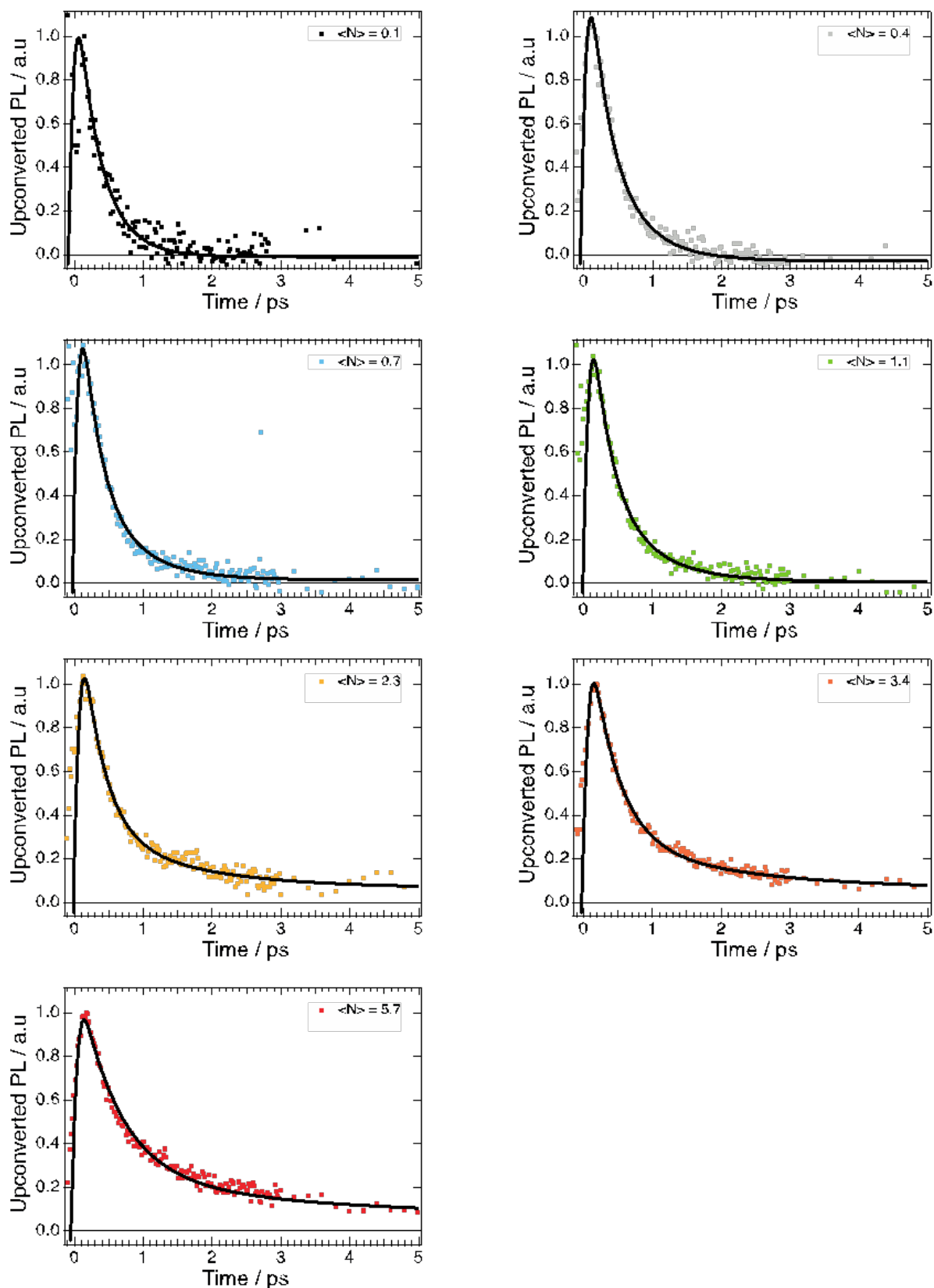


Figure S12. Normalized PL decays (dots) of the isolated band edge emission and best fits (lines) obtained according to the abovementioned procedure for $\langle N_{ex} \rangle = 0.1 - 5.7$.

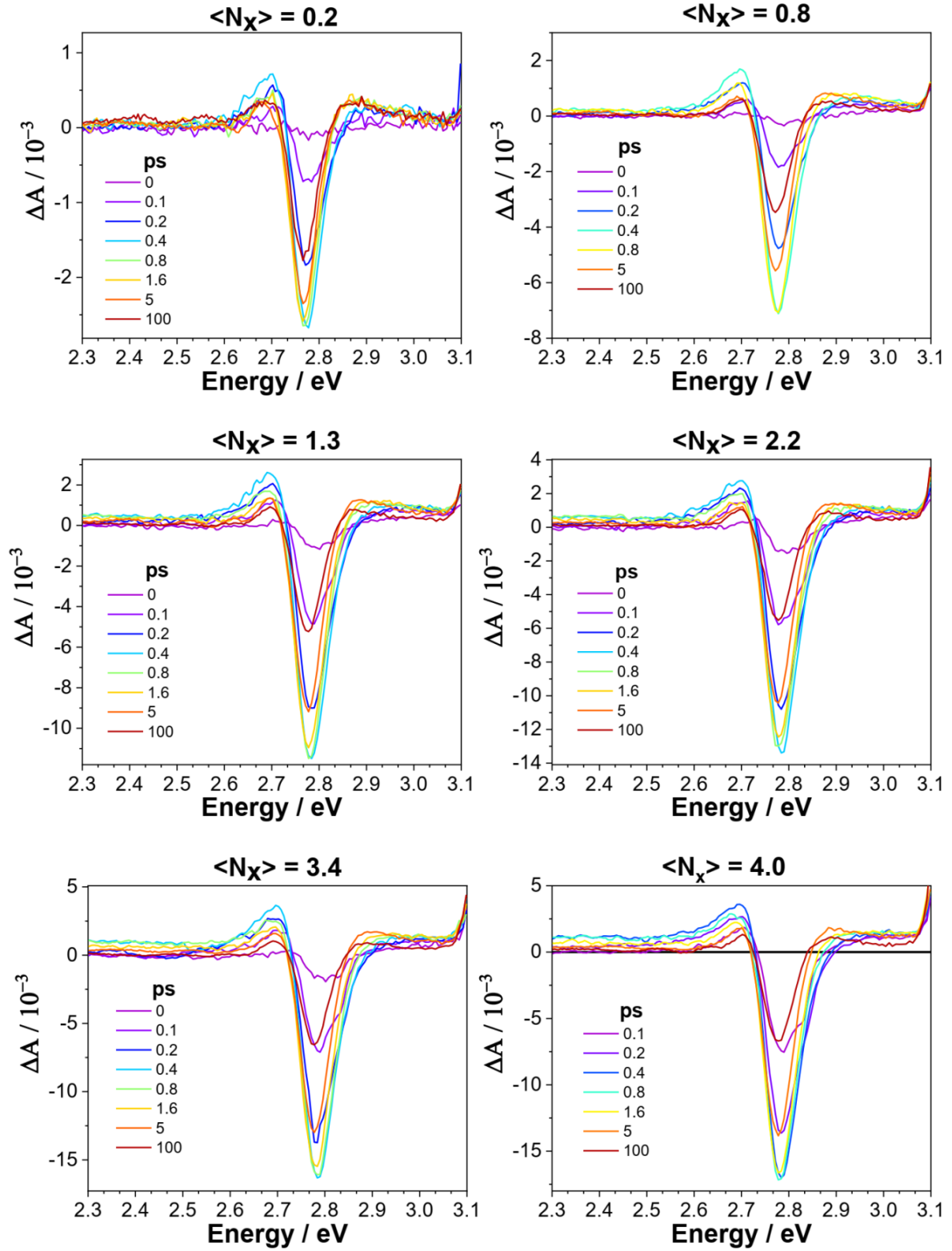


Figure S13. Normalized time-resolved emission spectral slices of CsPbBr₃ acquired by TA ($\lambda_{exc} = 390$ nm) for $\langle N_{ex} \rangle = 0.2 - 4$.

S6. Fitting of the PIA Band

We average the signal around 5 different wavelengths around the maximum to increase the signal over noise. We fitted the decay at each fluence with a double exponential function with a global fitting, in which time constants were linked to each other depending on the fluence and convoluted with a Gaussian function. The Gaussian width and time-zero were fixed, while All the time constants and amplitudes were left free. The IRF has been extracted from a 2D Gaussian fit using the cross-correlation between the pump and the probe at 390 nm.

Table S4. Extracted amplitude and lifetimes from the P fitting procedure for the PIA decay described above.

$\langle N_{ex} \rangle$	A_1	τ_1 / ps	A_2	τ_2 / ps	y_0
0.2	1.57	0.30 ± 0.02	0.002	2.51 ± 0.12	0.299
0.4	2.27	0.30 ± 0.02	0.026	2.51 ± 0.12	0.380
0.8	3.55	0.30 ± 0.02	0.105	2.51 ± 0.12	0.620
1.3	4.44	0.30 ± 0.02	0.196	2.51 ± 0.12	0.862
1.7	3.90	0.30 ± 0.02	0.595	2.51 ± 0.12	0.779
2.0	4.51	0.30 ± 0.02	0.777	2.51 ± 0.12	0.989
2.5	4.12	0.30 ± 0.02	1.01	2.51 ± 0.12	0.765
3.5	5.33	0.30 ± 0.02	1.26	2.51 ± 0.12	1.02
4.0	5.14	0.30 ± 0.02	1.54	2.51 ± 0.12	1.02

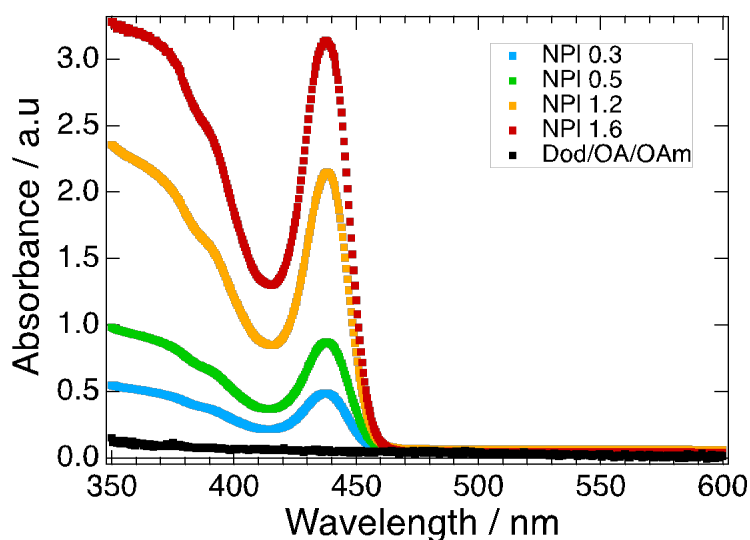


Figure S14. Absorption spectra of CsPbBr₃ NPIs solutions with different concentrations.

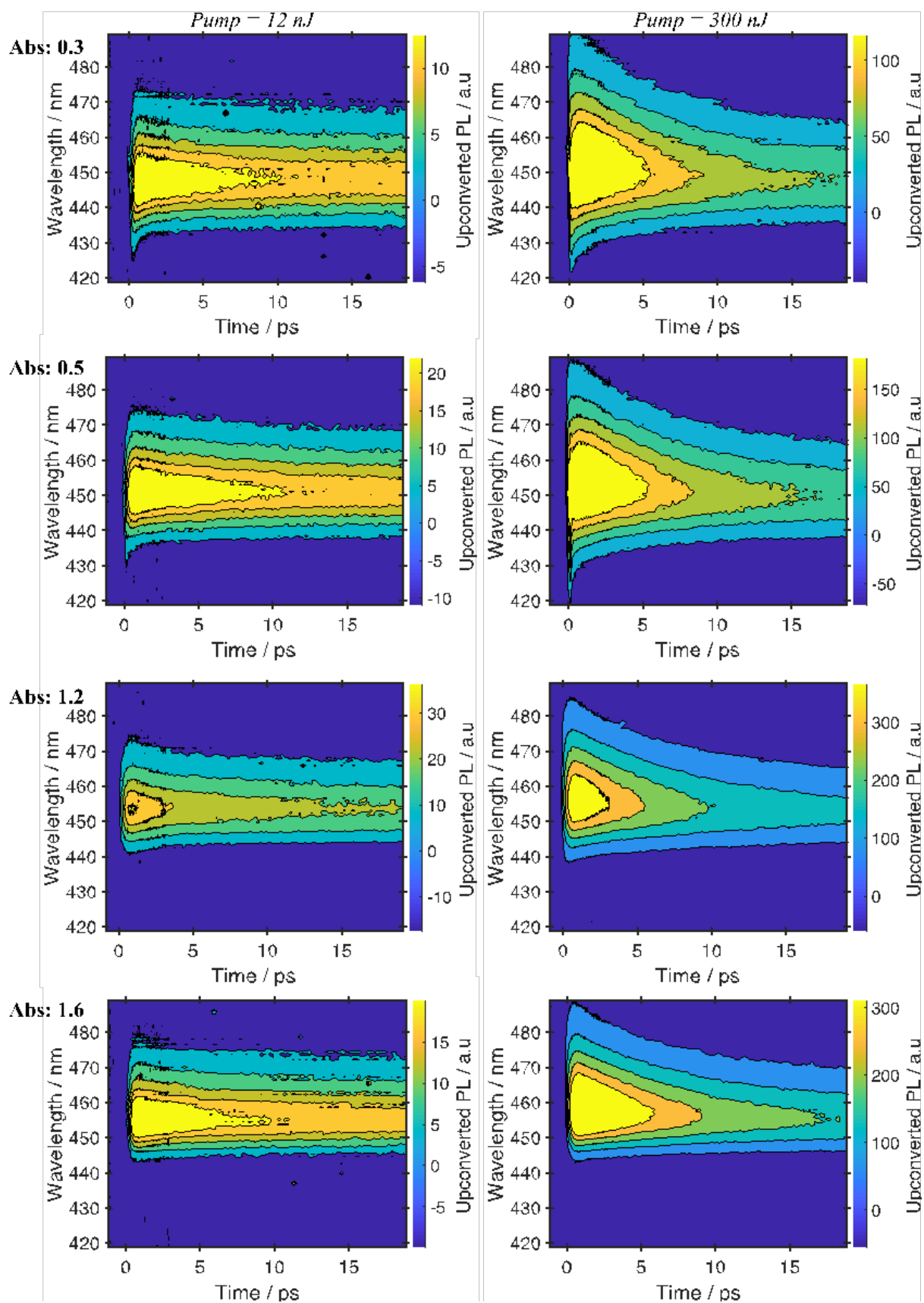


Figure S15. 2D time-resolved emission spectra of CsPbBr₃ solution with different concentration acquired by FLUPS ($\lambda_{exc} = 400$ nm) for pump energies of 12 nJ / pulse and 300 nJ / pulse.

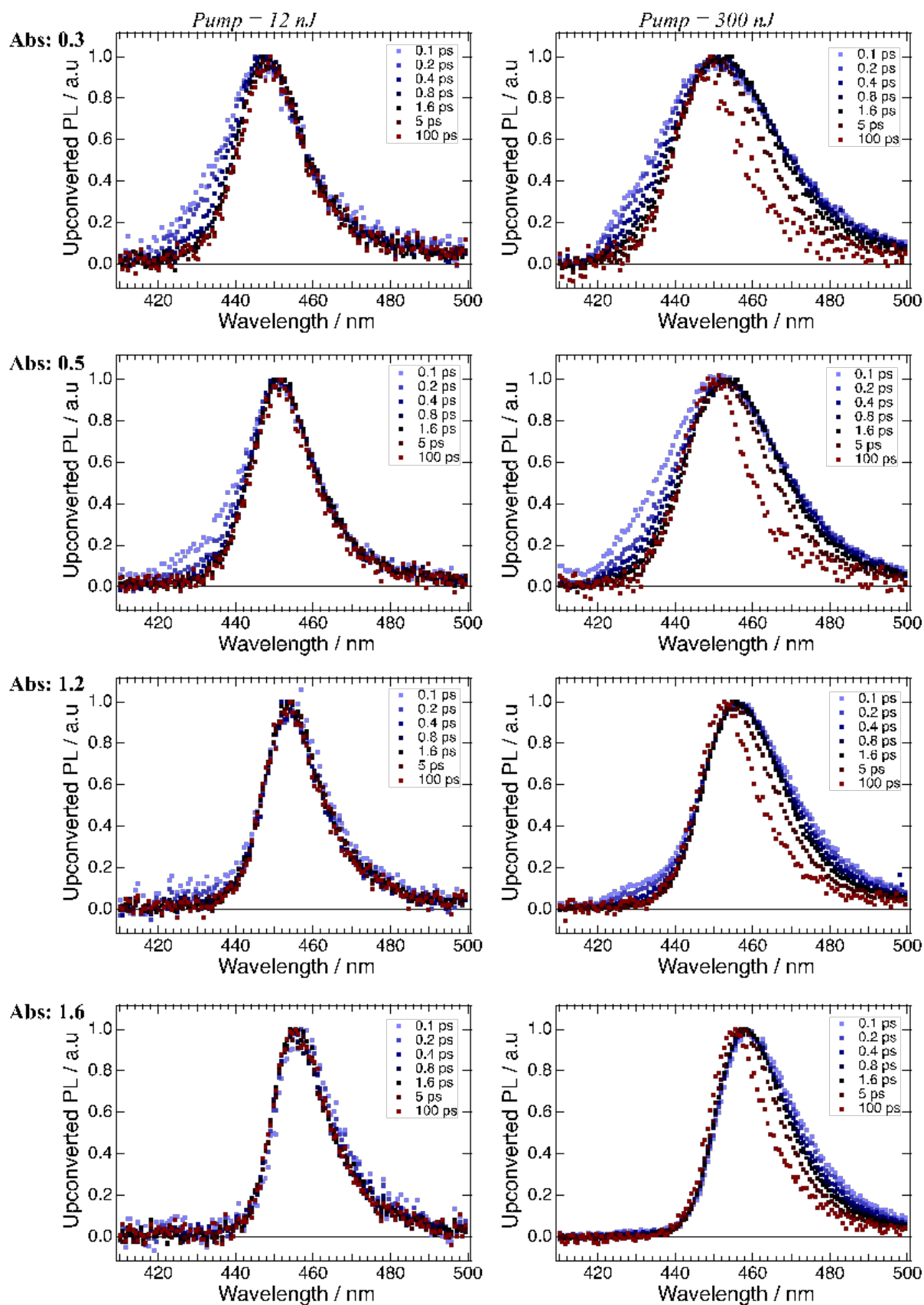


Figure S16. Normalized time-resolved emission spectral slices of CsPbBr₃ solution with different concentrations acquired by FLUPS ($\lambda_{\text{exc}} = 400$ nm) for pump energies of 12 nJ / pulse and 300 nJ / pulse.

S7. Calculation of the Mean Inter-Particle Distance

From the absorption cross-section obtained with Poisson statistics, we can deduce the concentration of NPIs in the cuvette with Equation S9-S10:

$$c = \frac{A}{\varepsilon l} = \frac{1000 \cdot \ln(10) \cdot A}{N_A \sigma l} \text{ [mol/L]} \quad (\text{S9})$$

$$N = \frac{c \cdot N_A}{10^3} = \frac{\ln(10) \cdot A}{\sigma l} \text{ [NPIs/cm}^3\text{]} \quad (\text{S10})$$

where A [-] is the absorbance, ε [cm²/mol] is the molar attenuation coefficient, l is the optical path length [cm], N_A [mol⁻¹] the Avogadro number and σ [cm²] the absorption cross-section. The mean inter-particle distance is then estimated by Equation S11:

$$\langle d \rangle \approx \left(\frac{1}{N}\right)^{\frac{1}{3}} \text{ [cm]} \quad (\text{S11})$$

Table S5. Extracted amplitude and lifetimes from the fitting procedure described above Table S2.

	NPI-0.5		NPI-1.2	
J / nJ per pulse	12	300	12	300
%A1	100	55	100	76
%A2	-	45	-	24
τ_1 / ps	0.32 ± 0.03	0.34 ± 0.02	0.26 ± 0.02	0.32 ± 0.01
τ_2 / ps	-	2.2 ± 0.11	-	2.1 ± 0.06
$\langle N_{\text{ex}} \rangle$ estimated	0.3	6.5	0.1	2.7

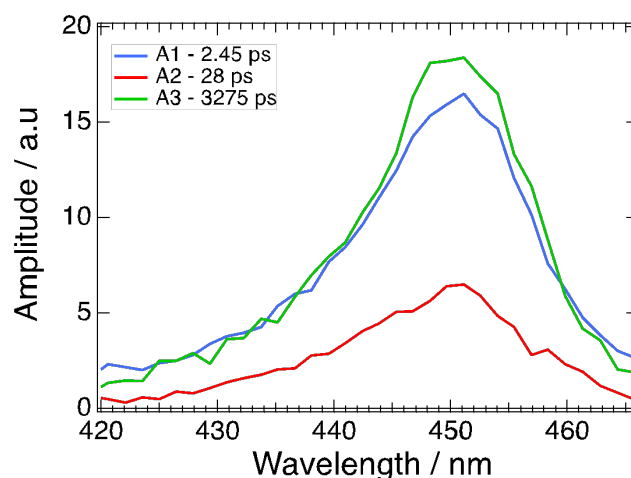


Figure S17. Decay associated spectra obtained by global fitting the FLUPS signal obtained for the highest concentration at the lowest fluence.

References

- [1] Vale, B. R. C.; Socie, E.; Burgos-Caminal, A.; Bettini, J.; Schiavon, M. A.; Moser, J.-E. Exciton, Biexciton, and Hot Exciton Dynamics in CsPbBr₃ Colloidal Nanoplatelets. *The J. Phys. Chem. Lett* **2019**, *11*, 387–394.
- [2] Schnabel, R. F.; Zimmermann, R.; Bimberg, D.; Nickel, H.; Lösch, R.; Schlapp, W. Influence of Exciton Localization on Recombination Line Shapes: In_xGa_{1-x}As/GaAs Quantum Wells as a Model. *Phys. Rev. B* **1992**, *46*, 9873–9876.
- [3] Leosson, K.; Jensen, J. R.; Langbein, W.; Hvam, J. M. Exciton Localization and Interface Roughness in Growth-Interrupted GaAs/AlAs Quantum Wells. *Phys. Rev. B* **2000**, *61*, 10322–10329.
- [4] Grim, J. Q.; Christodoulou, S.; Di Stasio, F.; Krahne, R.; Cingolani, R.; Manna, L.; Moreels, I. Continuous-Wave Biexciton Lasing at Room Temperature Using Solution-Processed Quantum Wells. *Nat. Nanotechnol.* **2014**, *9*, 891–895.
- [5] Li, Q.; Lian, T. Ultrafast Charge Separation in Two-Dimensional CsPbBr₃ Perovskite Nanoplatelets. *J. Phys. Chem. Lett.* **2019**, *10*, 566–573.
- [6] Mondal, A.; Aneesh J. Ravi, V. K.; Sharma, R.; Mir, W. J.; Beard, M. C. Nag, A.; Adarsh, K. V. Ultrafast exciton many-body interactions and hot-phonon bottleneck in colloidal cesium lead halide perovskite nanocrystals. *Phys. Rev. B* **2018**, *98*, 115418-115426
- [7] Makarov, N. S.; Guo, S.; Isaienko, O.; Liu, W.; Robel, I.; Klimov, V. I. Spectral and Dynamical Properties of Single Excitons, Biexcitons, and Trions in Cesium–Lead–Halide Perovskite Quantum Dots. *Nano Lett.* **2016**, *16*, 2349–2362.